

---

# Analysis of Shock and High-Rate Data for Ceramics: Strength and Failure of Brittle Solids

## Report

by  
Dennis E. Grady

Prepared for  
U.S. Army TARDEC  
Emerging Technologies Team

July 2007

Contract No. W56HZV-05-P-L682

ARA Project No. 17168

**Applied Research Associates, Inc.**  
4300 San Mateo Blvd. NE, Suite A-220  
Albuquerque, New Mexico 87110  
(505) 883-3636



<b>REPORT DOCUMENTATION PAGE</b>			<i>Form Approved</i> <b>OMB No. 0704-0188</b>		
Public reporting burden for this collection of information is estimated to average 1 hour per response, including the time for reviewing instructions, searching existing data sources, gathering and maintaining the data needed, and completing and reviewing this collection of information. Send comments regarding this burden estimate or any other aspect of this collection of information, including suggestions for reducing this burden to Department of Defense, Washington Headquarters Services, Directorate for Information Operations and Reports (0704-0188), 1215 Jefferson Davis Highway, Suite 1204, Arlington, VA 22202-4302. Respondents should be aware that notwithstanding any other provision of law, no person shall be subject to any penalty for failing to comply with a collection of information if it does not display a currently valid OMB control number. <b>PLEASE DO NOT RETURN YOUR FORM TO THE ABOVE ADDRESS.</b>					
<b>1. REPORT DATE</b> 07/31/2007		<b>2. REPORT TYPE</b> Final		<b>3. DATES COVERED</b> (From - To) August, 2005 – August, 2006; April, 2007	
<b>4. TITLE AND SUBTITLE</b> Analysis of Shock and High-Rate Data for Ceramics: Strength  and Failure of Brittle Solids			<b>5a. CONTRACT NUMBER</b> W56HZV-05-P-L682		
			<b>5b. GRANT NUMBER</b>		
			<b>5c. PROGRAM ELEMENT NUMBER</b>		
<b>6. AUTHOR(S)</b> Grady, Dennis, E			<b>5d. PROJECT NUMBER</b> 17168		
			<b>5e. TASK NUMBER</b>		
			<b>5f. WORK UNIT NUMBER</b>		
<b>7. PERFORMING ORGANIZATION NAME(S) AND ADDRESS(ES)</b>  Applied Research Associates, Inc. 4300 San Mateo Blvd, NE Ste A-220 Albuquerque, NM 87110			<b>8. PERFORMING ORGANIZATION REPORT NUMBER</b>		
<b>9. SPONSORING / MONITORING AGENCY NAME(S) AND ADDRESS(ES)</b> U S Army Tacom 6501 E. 11 Mile Road Warren, MI 48397-5000			<b>10. SPONSOR/MONITOR'S ACRONYM(S)</b> TARDEC		
			<b>11. SPONSOR/MONITOR'S REPORT NUMBER(S)</b>		
<b>12. DISTRIBUTION / AVAILABILITY STATEMENT</b>  <b>DISTRIBUTION STATEMENT A.</b> Approved for public release; distribution is unlimited.					
<b>13. SUPPLEMENTARY NOTES</b>					
<b>14. ABSTRACT</b> <p>Ceramics based on composition of the light intermetallic compounds, have demonstrated considerable success as a barrier material in armor applications. The exceptional strength-to-density ratio of ceramic plays a crucial role in the positive performance of ceramics in the terminal ballistic environment. Even the higher density ceramics, such as tungsten based materials, show promising behavior in space-limited armor applications.</p> <p>The implementation, optimization and evaluation of ceramic in armor systems benefit from the rapidly growing power of computational analysis and simulation. Production codes such as EPIC. CTH, ALE-3D, among others, are making large strides toward the accurate and efficient simulations of the wide-ranging armor and anti-armor applications of concern.</p> <p>Central to the confident computational simulation of the performance of ceramics in the terminal ballistic environment is, of course, material response models, which describe the</p>					
<b>15. SUBJECT TERMS</b>					
<b>16. SECURITY CLASSIFICATION OF:</b> U			<b>17. LIMITATION OF ABSTRACT</b>  UU	<b>18. NUMBER OF PAGES</b>	
<b>a. REPORT</b> UU	<b>b. ABSTRACT</b> UU	<b>c. THIS PAGE</b> UU			<b>19a. NAME OF RESPONSIBLE PERSON</b> Dennis Grady
					<b>19b. TELEPHONE NUMBER</b> (include area code) 505-883-3636



---

## Acknowledgments

The author wishes to thank attendees of the several meetings hosted during this program year, on topics of ceramic armor materials testing and development, for providing stimulus for the work reported here. In particular, the author thanks Lisa Prokurat-Franks, Douglas Templeton, Timothy Holmquist, Gordon Johnson, Datta Dandekar, Murli Mangnani, Xin Sun, Charlie Anderson and Dennis Orphal for their respective incentives and input.

The author also wishes to thank Tracy Vogler and Lalit Chhabildas at Sandia National Laboratories for continuing discussions on topics of this report and Craig Doolittle and Terry Caipen at Applied Research Associates for technical help on several parts of the report. Partial support for the present research was also provided by Sandia National Laboratories through the DOE/DOD MOU Munitions Technology Development Program.

# Table of Contents

<b>I</b>	<b>Introduction and Summary .....</b>	<b>1</b>
	Introduction .....	1
	Summary .....	2
<b>II</b>	<b>Background.....</b>	<b>5</b>
<b>III</b>	<b>Progression of Strength and Failure Models .....</b>	<b>7</b>
	Observations of Failure wave Phenomena .....	7
	A Meso-Kinetic Model of Delayed Failure .....	9
	Relationship of Physics Based Model to Other Studies .....	21
<b>IV</b>	<b>Impact Breach of Glass and Ceramic Plate.....</b>	<b>23</b>
	The Ballistic Model.....	23
	Failure Criterion .....	27
	Experiments on Impact Breach of Float Glass.....	29
	Failure Toughness of Glass Plate.....	30
	Post-Failure Fracture Damage.....	31
	Residual Projectile Velocity.....	34
<b>V</b>	<b>Fragmentation of Ceramics .....</b>	<b>35</b>
	Hydrodynamic Turbulence .....	35
	Catastrophic Fracture .....	36
<b>VI</b>	<b>Closure .....</b>	<b>40</b>
<b>VII</b>	<b>References .....</b>	<b>42</b>

# I Introduction and Summary

The U.S. Army is considering high quality ceramics prepared from light inter-metallic compounds as engineering materials for armoring vehicles against kinetic energy threats. Application of ceramics within armor systems requires a full understanding of the physical and mechanical response of ceramics to the range of impact and penetration conditions of concern. The present report documents continued work in support of the TARDEC/ARL efforts on this topic.

## *Introduction*

The project effort reported on here is a continuing study undertaken to collect, survey, analyze and model shock-wave and other related high-rate data available for candidate armor ceramics with emphasis on response in the ballistic environment. Ceramics considered here include the various light inter-metallic compounds selected by the Army for consideration such as silicon carbide and aluminum oxide, as well as other ceramics and glasses currently being pursued by TARDEC with high potential for armor applications.

The TARDEC/Army Research Laboratories program in armor ceramics currently involves a number of efforts at various facilities including materials research, experimental studies and computational modeling. Thus, the present effort focuses on available data, analysis approaches and theoretical concepts, not currently under consideration at other laboratories, which best complements and furthers goals of the current TARDEC program.

The present effort also includes physics-based modeling of the response of ceramics under impact and penetration for purposes of furthering computational modeling of ceramics in armor applications. This supporting theoretical effort serves both the furthering of computational models, and the analysis and interpretation of data necessary to benchmark the models. Both objectives fall within the tasks of the present project.

New physics-based models of ceramic response under shock and high-rate loading are presented here. Emphasis is on, but not restricted to, the influence of microstructure and mesostructure on the high-rate and shock-compression response of ceramics experienced in the armor applications events. Such microstructure and mesostructure result from a range of heterogeneities in polycrystalline solids, including porosity and second phase material. Data emphasizing these microstructure features for the ceramics of current interest to TARDEC are presented. These data are evaluated within the framework of the new physics-based models. Results of these efforts contribute directly to material response properties necessary for computational modeling and simulation of armor applications involving ceramic components.

Several specific theoretical and modeling efforts are also undertaken in the present study. These efforts have several objectives: One objective is to clarify the regimes and character of shocks in the ballistic impact environment. This modeling study provides focus for

exploration of ceramic strength in the ballistic event – in particular the failure, or fracture, wave phenomena. Another objective is the examination of size scaling in the catastrophic failure of brittle solids. This issue relates to the selection of material properties in the response models which adequately capture the observed scaling behavior.

The present effort culminates with a new approach to the modeling of strength and failure of brittle solids such as glass and ceramics. Although not yet completed here in detail, some of the essential features are described, and directions for further study are outlined.

## Summary

The principle thrust of this effort continues to be the collection, assessment and presentation of shock-wave and high-strain-rate data on ceramics and ceramic-like materials in support of the U.S. Army TARDEC/ARL program on vehicle armor development. The emphasis focuses on characterization of dynamic material response within the armor impact and penetration environment for purposes of computational and engineering model assessment. Progress towards this end is summarized here and described in detail within the remainder of the report.

Modeling of ceramic and glass has continued in the present program year. Time dependent or delayed failure of ceramic and glass are evident in planar shock experiments and may play a significant role in the ballistic impact event including dwell and penetration resistance. A theoretical model of failure of brittle materials based on kinetics of mesoscopic fracture is pursued this year. The impact resistance of ceramic and glass plate have application to transparent and appliqué armor. A model, which enlightens the size scale dependence and the time dependent strength of armor plate, is developed in support of computational modeling efforts. The strength of failed ceramic in the penetration environment is a key contribution to the ballistic resistance and is not well understood. Theoretical efforts are pursued to better understand the character of the failed and comminuted ceramic including fragment size and distribution.

Specifically, the following accomplishments are documented in the present report:

- An accumulation of experimental evidence over approximately the last two decades including quite recent experimental results [Vogler *et al.*, 2006] suggests a transient strength and time-delayed failure of brittle solids including those ceramics and glass with armor application potential. A survey of the evidence for the strength and failure behavior is undertaken and the underlying responsible physics is explored. A physical behavior governed by time-dependent equilibration of a mesoscopic stress state following transient loading is proposed. A physics-based and statistical meso-kinetics model is developed. A preliminary application of the model provides a credible and physically satisfying prediction of delayed failure, or failure wave, behavior for shock loaded soda-lime glass.

Some relationships of the present model with recent research at Rutgers University [Niesz, 2005] and computational model development and validation [Holmquist and Johnson, 2006] are discussed.

- This study further pursues theoretical analysis and modeling of impact failure and breach of ceramic and glass plate subject to high-speed fragment impact. An analytic representation of the impact momentum transfer provides a relation for the time-dependent shear stress suffered by the brittle plate on impact. A Tuler-Butcher failure criterion [Tuler and Butcher, 1968] based on the time history of the shear stress provides in turn a plate breach criterion. Within the Tuler-Butcher framework, breach criteria based on stress, on work, or on impulse exhibit increasing degree of non-replica scaling.

Recent data [Sun et al., 2006] delineating the onset of failure of glass plate subjected to impact of steel spherical projectiles are ideal for exploring the impact physics uncovered with the theoretical model. The data are best described by a work (or energy) based Tuler-Butcher failure criterion. Failure exhibits non-replica scaling decreasing as the square root of the system size.

The critical Tuler-Butcher constant fit to the glass failure data has dimensions of energy. Consequently, the constant can be expressed in units of fracture toughness (called here the failure toughness) and compared with the standard fracture toughness of glass. A failure toughness of glass plate of  $25.9 \text{ MPa m}^{1/2}$  is determined by the data, differing starkly from the approximately  $0.5\text{-}1.0 \text{ MPa m}^{1/2}$  fracture toughness for glass. Thus, a two-strength property of glass plate governs failure and breach of the plate on one hand, and accumulation of fracture damage in the glass on the other.

The theoretical model is extended to predict the extent of radial fracture damage subsequent to impact breach of the glass plate. Fracture toughness of the glass and the rate of loading imparted by the impact are used to calculate the number and propagation distance of radial fractures.

Lastly, the model is used to calculate the residual velocity of projectile and leading debris following breach of the glass plate.

- The study also initiates an effort explain underlying physical principals of impact fragmentation of ceramics with focus on support of improved computational modeling of post-failure resistance of comminuted ceramic in the terminal ballistic event. Failure of ceramic in the ballistic event involves pervasive brittle fracture and fragmentation of the high-strength material. Ballistic resistance of ceramic involves the strength up to failure, and the continued strength through and beyond the fracture and fragmentation stages of the response. Physics-based modeling of the ceramic response for purposes of predicting ballistic events requires physical understanding of the nature of the dynamic fracture and fragmentation behavior of the brittle solids.

This effort points out an elucidating parallel between catastrophic fragmentation of brittle solids and hydrodynamic turbulence in fluids. The analogy clarifies the size



scale invariance and power-law behavior of observed fragment size distribution of comminuted ceramic over much of the range of the distribution. From this understanding, a clearer comprehension of the form of the particle distribution is emerging. A functional form for the fragment distribution is proposed and explored with available data. Improved characterization of the failed ceramic will better support strength and shear resistance modeling of impact degraded ceramic materials. This latter theoretical study is preliminary and will continue in the following program year.

- Presentations of the current program progress have been made at the following project meetings:
  - Working Group Meeting, Sandia National Laboratories, Albuquerque, New Mexico, December 5-6, 2005.
  - Army Research Office Workshop, Washington DC, February 14-15, 2006.
  - Working Group Meeting, Purdue University, West Lafayette, Indiana, June 21-22, 2006.

A paper on Dynamic Strength of Ceramics was presented at the International Plasticity Conference, Halifax, Nova Scotia, July 17-21, 2006.

## II Background

The benefits of using computers to simulate the interactions of weapons and armor systems are readily apparent. Economics and system/materials optimization are among the obvious benefits. There are challenges, however, which must be overcome before such computational tools become fully reliable and can realize the many available benefits. Namely, the description of materials and their response within the extreme terminal ballistic environment must be faithful.

Similarly imaginative engineering models based on good physical understanding of the ballistic phenomena have, and will continue to have, an important role in the assessment of armor and weapon performance.

In both computational and engineering endeavors the dynamic material response and the constitutive models describing material response over the range of deformations and thermodynamic conditions experienced must be fully understood and adequately characterized.

Within the present effort, these issues are restricted to ceramics and ceramic-like materials, and their role as armor components within the armor/anti-armor terminal ballistic event. The physics of failure and deformation of brittle solids such as ceramics and glass within the terminal ballistic environment is not yet fully understood. Phenomenological behaviors such as dwell, failure waves, fracture kinetics and phase transformation are still topics of active research. Consequently, computational constitutive models developed to describe the response of ceramic materials in armor applications must be viewed as tentative. Nonetheless, considerable progress is continually being made on such model development [e.g., Holmquist and Johnson, 2002] and improvements can be expected to continue.

Engineering ceramics are commonly complex polycrystalline solids in which detailed chemical and material processing methodologies have been developed and pursued to enhance specific properties critical to the intended system performance. This careful tailoring of ceramic properties to improve performance is rapidly maturing in the armor application of ceramics. Microstructure features such as porosity, second phase material, controlled anisotropy, and so forth, are increasingly being recognized as either detrimental to, or an enhancement to, armor performance under specific conditions.

Even transparent glass, which emerges as an important armor material of interest in this report, when examined on an adequately small length scale exhibits a stress concentrating defect structure which must play a role in the strength and ultimate failure of glass and glass bearing structures.

One difficulty arises in determining constitutive models which adequately describe the dynamic response of the new materials in computer simulations of ballistic events. The cost in time and resources, which would be necessary to perform the usual suites of material properties tests on new materials of interest, becomes rapidly exorbitant. It therefore

becomes necessary to pursue other, more expedient, methods to estimate sensible response models.

It is possible, in certain cases, to adequately estimate equation of state and dynamic strength properties of more complex engineering materials through appropriate mixing or extrapolation/interpolation of the properties of this material's simpler component materials. For example, it is possible to make reasonable estimates of the equation of state and strength of a porous ceramic if the corresponding properties of the monolithic ceramic are available. Or, as another example, when appropriate properties of component materials are known, sensible descriptions of the constitutive equation of state of a ceramic mixture of these components can be determined.

Within the charter of the present program of surveying and analyzing earlier shock-wave and high-rate data for armor ceramics, analysis and theoretical modeling is continued with emphasis on extracting information from these earlier data that are relevant to the physical understanding and modeling of the ballistic event. Both recently developed, and earlier, but not commonly known, analysis and theoretical approaches are pursued. Applications of the theoretical efforts and analysis are examined in light of available data for ceramics and glass.

### III Progression of Strength and Failure Models

The section explores physical theories and models in pursuit of a better understanding of the strength and failure behavior of brittle materials in the shock wave and ballistic environment with the objective of developing better fidelity physical and computational response models. In particular the physics underlying failure wave phenomena are investigated and a framework for a physics- and statistics-based model of failure is proposed. Some relationships of this model to recent work by others are talked about.

#### *Observations of Failure wave Phenomena*

It has become common in recent years to identify the observed delay in fracture failure, after passage of the shock wave, as a failure wave [Kanel *et al.*, 1992]. Earlier manifestations of the fracture kinetic phenomena were observed in a number of brittle materials. In certain hard rock materials, with compressive and fracture strengths comparable to current ceramics, the existence of upper and lower failure surfaces have been observed due to the delaying kinetics of fracture. These strength features lead to an effective rate dependent, or time dependent, failure under shock and high-rate loading [Grady *et al.*, 1977; Grady, 1995; Grady, 1998]. Brannon *et al.* (1983) observed a process of coarse shear failure features following initially elastic shock compression in single crystal quartz and lithium niobate crystals with high resolution photography. Earlier Soviet work inferred the existence of a fracture wave phenomena in the high velocity penetration of brittle solids (*e.g.* Galanov *et al.*, 1989).

Kanel *et al.* (1992) provided the first clear evidence on the nature of the stress state in brittle materials accompanying the failure-wave fracture process behind the shock wave. Kanel *et al.* used normal- and transversely-oriented piezo-resistive stress gages to monitor the corresponding stress in glass, and recorded the marked loss in stress difference as the delayed fracture process proceeded within the failure wave. Since this seminal study, a marked acceleration in experimental activity has focused on this topic in attempting to better understand its unique dynamic failure features. In spite of this focus of activity, the underlying physics governing the failure wave phenomena are still far from clear.

High speed photography [Brannon, 1983; Bourne, *et al.*, 1994] has provided compelling evidence for the delayed failure wave and fracture kinetic phenomena. Other diagnostics are needed, however, to assess stress and deformation features within the failure event. A complementary diagnostic is provided by the orthogonal stress gages measurements of Kanel *et al.* (1992) on glass, and velocity interferometry records obtained in the shock loading of soda-lime glass [Grady and Chhabildas, 1997]. The stress profiles of Kanel *et al.* in Figure (1) show an initial abrupt rise of the longitudinal and transverse stress to markedly different amplitudes suggestive of elastic response of the glass under the uniaxial-strain shock-wave loading. The recorded stress difference behind the initial shock provides a measure for calculating the strain energy stored in elastic distortion. Failure through shear

fracture appears to occur several microseconds after passage of the shock wave as suggested by a rapid drop in stress difference and is accommodated principally by a marked rise in the lateral stress amplitude.

Free surface velocity histories recorded with VISAR diagnostic methods induced through shock wave loading of soda-lime glass are shown in Figure (2) and bear little resemblance to the profiles of Kanel *et al.* Velocities at a free surface are, however, far removed from the in-material measurement of stress histories. It is also important to remember that piezo-resistive gages span a sensible area within the test sample. Such gages encompass several millimeters or more and presumably measure a reasonable average stress over the area subtended. In contrast, the VISAR diagnostic is closer to a point measurement with laser spot diameter usually considerably less than a tenth of a millimeter.

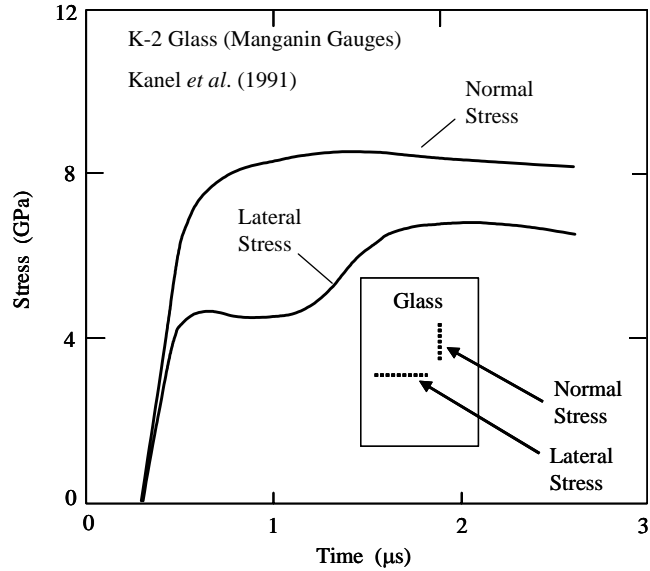


Figure 1: Manganin stress gage measurements of normal and lateral stress in K-2 glass [Kanel *et al.*, 1991].

Attention is focused on the two lowest amplitude profiles in Figure (2), and the two rather chaotic looking VISAR records next higher in amplitude. These two sets of records correspond to shock stress amplitudes of about 4.5 GPa and 6.5 GPa, respectively; well within the 4–7 GPa range that other workers have suggested failure wave behavior in soda-lime glass. The successively higher stress amplitude tests presumably exceed the shock amplitude at which the glass transitions to a homogenous Hugoniot-elastic-limit and post-HEL yield behavior. The two profiles at about 6.5 GPa suggest failure through a coarse fracture process in regions reasonably close to the front of the shock near the point of the VISAR measurement. The lower amplitude profiles suggest nominal elastic response of the glass to the 4.5 GPa shock stress level. The gradual drop in velocity, of about 25 to 35 m/s, behind the shock front hints at more complex processes occurring, however. This relaxation in velocity prior to any expected release wave suggests a modest drop in longitude stress and corresponding increase in the specific volume strain

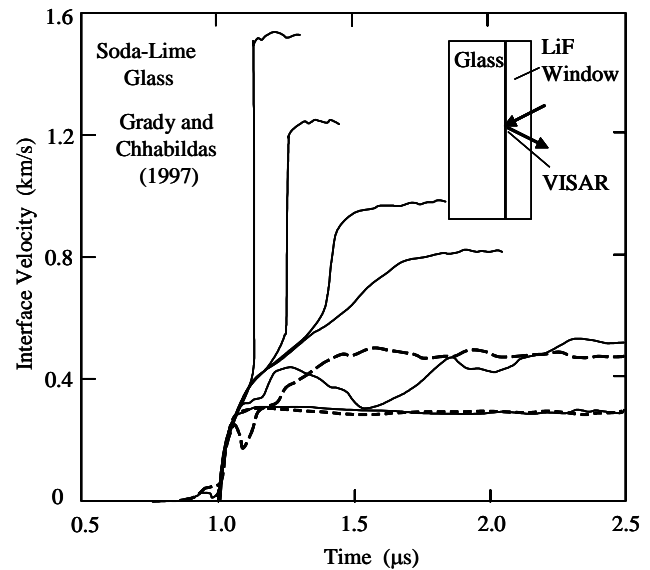


Figure 2: Interface velocity interferometer (VISAR) measurements on soda-lime glass [Grady and Chhabildas, 1997].

(~10%). It is reasonable to speculate that the observed behavior is a consequence of delayed shear fracture induced dilation brought about by the failure process some time after passage of the shock wave.

## *A Meso-Kinetic Model of Delayed Failure*

A physically satisfying theory of the dynamic failure of brittle solids should include two principal features. First, the theory should provide an explanation of the underlying physical character of the material that gives rise to this unique dynamic failure behavior. Second, this character of the material should be imbedded within a physics-based model that leads to a satisfactory description of the observed behavior of dynamic failure in brittle solids. Such failure behavior should include the shock wave stress and velocity data for glass discussed previously, as well as a host of other strength and failure properties unique to brittle solids. A theory of strength in brittle solids is developed in the following sections that attempts to address the two questions posed.

### **Material Features Governing Failure in Brittle Solids**

The theory that will be pursued will be called a meso-kinetic theory of the strength of brittle solids. As will be shown, this name is descriptive of the material aspects of the underlying physics to be proposed. The single key attribute of brittle solids, which must be accepted before pursuing the theory, is that when a brittle solid is subjected to a mechanical load, there is a long-range (meso-scale) correlation of the induced stress and elastic strain field at any point in the body. That is, the stress at a material point depends not only on properties of the material at that point, but also on properties in some mesoscopic neighborhood of that point. The spatial extent of this correlation length is not yet fully understood, but for a granular solid it is envisioned to be tens of grains, and perhaps as much as hundreds of grain or more. This premise is assumed to apply to amorphous brittle materials as well.

To further illustrate the stress state and meso-scale correlation within a brittle body, consider a cylindrical specimen of such a solid (ceramic, glass, concrete, competent rock). Subject the sample to a uniform static axial load within the elastic limits of the material, and further confine the specimen to zero lateral motion. In response to this loading, a macroscopic axial stress  $\sigma_x$  and lateral stress  $\sigma_y$  will be developed in the body to support the elastic deformation. This uniaxial loading is appropriate since we will shortly consider subjecting the same sample to shock wave loading under which the same global stress conditions are achieved.

Imagine a line or trace interior to the sample across the diameter along which the stress is monitored on increasingly finer length scales as illustrated in Figure (3). Only the deviator stress  $\tau$  is of interest, since this will be considered as the stress driving fracture in the theory. Following from the premise a long range correlation of the local stress state, it is expected that, at some sufficiently small length scale, variations in the local stress state  $\tau$  from the homogenous or average stress  $\bar{\tau}$  will occur. As the length scale over which stress is monitor

becomes even finer, fluctuations in the local stress state will become increasingly chaotic and probably fractal in character. It is fluctuations in the local stress deviator over the mesoscopic range of perhaps tens of micrometers to millimeters that lie at the heart of the present theory. (This range can, of course, extend much further in more heterogeneous materials such as concrete or rock media.)

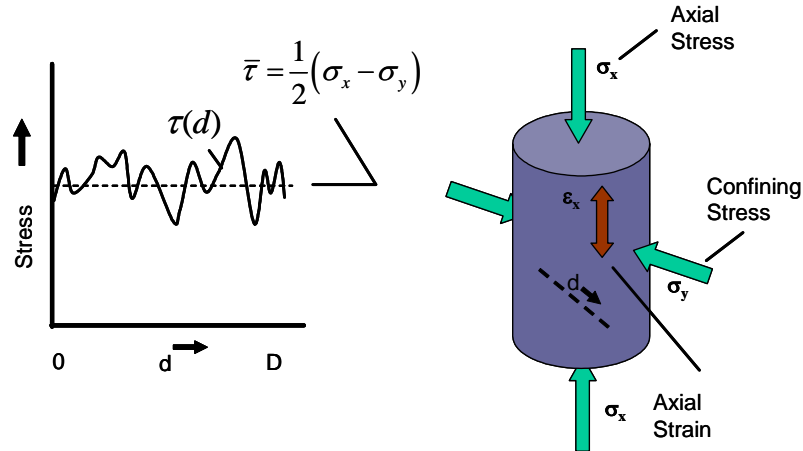


Figure 3: Illustrates variations of the local shear stress state due to meso-scale heterogeneities in material properties.

What are the sources leading to the long range correlations of the stress at a material point and the corresponding variations of this local stress from the average? These sources will not be quantified at this juncture, but qualitatively it lies within all of the imperfections inherent to engineering materials. Such imperfections include features such as impurities, chemical inhomogeneities, porosity, second phase, internal strains, and granular correlations along with hosts of others.

The present theory will show that the dynamic mesoscopic response of the material is responsible, at least in part, for the unique time-dependent failure behavior observed for brittle solids. It follows that this mesoscopic character must be a property of the material and, as such, measurable by some independent means. Some possible methods for experimentally assessing this meso-scale property of the material will be explored in a later section.

The existence of a mesoscopic stress field with long-range (mesoscale) stress correlations has potential implications to several strength features of brittle solids. Brittle solids are noted for exhibiting a size dependent strength when self-similar structures are subjected to similar loads to the point of failure. Size dependent strength might be expected when the zone of failure onset within the loaded body becomes comparable in size to correlation length scales in the mesoscopic stress field. This phenomenon relating to the strength of brittle solids can be pursued further within the context of the present theory. This pursuit is not, however, central to the thesis of the present study. It is brought forth here, because when size dependence is noted in strength tests such as indentation hardness or triaxial compression, there are possibilities of relating such data to dynamic strength through the present theory.

Another strength feature, and the one that is central to the present development, is that of the failure of brittle solids subjected to strong shock waves. When a sharp shock passes through a brittle solid resulting in a continuum axial and lateral stress,  $\sigma_x$  and  $\sigma_y$ , comparable to that of the statically loaded specimen discussed earlier, the same mesoscopic stress field is not immediately achieved. There is instead a time dependence to the stress field as equilibration over the mesoscale correlation length scales is achieved. This equilibration process lies at the heart of the present meso-kinetic theory, and is pursued in further detail in the sections ahead.

## Fracture at the Mesoscale

Fracture after passage of the shock wave will initiate at fracture producing flaws. A Griffith flaw is commonly considered in linear elastic fracture mechanics, and stresses in the neighborhood of the Griffith crack are written as [e.g., Freund, 1990 ],

$$\sigma_{ij}(r, \theta) \approx K \frac{f_{ij}(\theta)}{\sqrt{r}}, \quad (1)$$

The parameter  $K$  is the stress intensity factor and in the present application, is written  $K \approx \tau\sqrt{d}$  where,  $d$  is the crack dimension and  $\tau$  the neighboring shear stress field. Depending on the crack orientation,  $K$  is some mix of mode II and mode III stress intensity [Lawn, 1993] in the present application. The brittle material strength and local heterogeneity would probably accommodate some mode I stress intensification, which would lessen as the confining pressure was increased. Mode I stress intensification will be ignored here.

When the same Griffith crack is subjected to an instantaneous application of the stress  $\tau$ , the stress intensity factor is time dependent with the form shown in Figure (4). At early times the stress intensity increases with time according to  $K \approx \tau\sqrt{ct}$ . At late times  $K$  equilibrates to the static value  $K \approx \tau\sqrt{d}$ . A critical stress intensity factor  $K_c$ , at which inelastic growth of the fracture initiates, is identified as a property of the material. Fracture at the flaw initiates when  $K$  achieves  $K_c$ , either during quasistatic elevation of  $\tau$ , or during the time-dependent amplification of  $K$ .

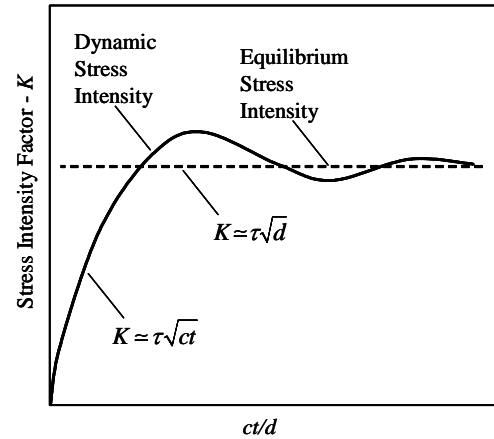


Figure 4: Dynamic stress intensity factor.

Response of the same flaw within the mesoscopic stress field postulated for brittle solids is more complex. Stress concentration in the neighborhood of the flaw is still determined by the neighboring shear stress  $\tau$ . However,  $\tau$  depends in turn on the far field stress  $\bar{\tau}$ , and on details of the material structure within some mesoscale correlation length  $a \gg d$ . When subjected to a near instantaneous stress load, such as passage of a shock wave, time-



dependent equilibration of the stress intensity factor over both the flaw and the near-field structure within the correlation length  $a$  must be accommodated. We propose the more general time dependence of the stress intensity,

$$K = \bar{\tau} (ct)^n. \quad (2)$$

The power  $n$  is expected to be somewhat less than one-half, reflecting the slower late-time equilibration over the mesoscale structure of dimension  $a$ . Stress intensity equilibrates at  $K \simeq \bar{\tau} a^n$  and fracture initiates if a critical stress intensity  $K_c$  is exceeded.

The dimensions of the stress intensity in the present development are not the same as resulting from the square root singularity of a Griffith flaw. This more general stress intensity and failure criterion has similarities to the development of Mott (1947) and relates closely to Weibull characterization of the strength of solids [*e.g.*, Weibull, 1951].

Plots of the stress intensity, which parallel the Griffith square root singularity of Figure (4), is shown in Figure (5). The comparable early time amplification of the stress intensity, but reduced rate of intensification at later time, is consistent with the expected equilibrium behavior over the mesoscopic length scale, and is reflected by the model.

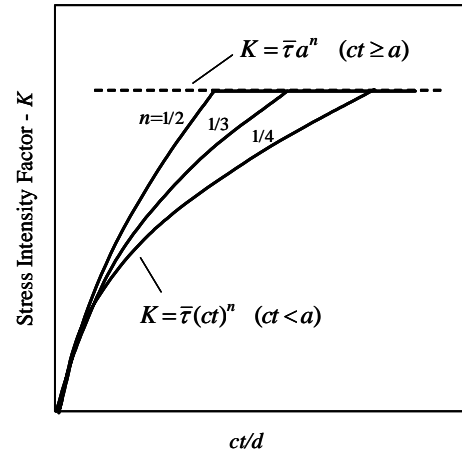


Figure 5: Generalized power-law stress intensity with time-dependent and equilibrium regions.

## Statistical Description of Mesoscopic Fracture

Thus, fracture producing defects, and the stress activation of those defects, depends not only on the strength of the impressed stress field  $\bar{\tau}$ , but also on the character of an overlying microstructure-dependent mesoscopic stress field. In the neighborhood of the defect, stress intensity is controlled by a correlation length scale  $a$  and an intensification power  $n$ , which are both properties of the mesoscale field. These parameters are expected to differ at each fracture site of concern. The correlation length scales of the mesoscopic field at fracture sites will be assumed Poisson distributed, with probability density,

$$p(a) = \frac{1}{a_o} e^{-a/a_o}, \quad (3)$$

and that the intensification power  $n$  is nominally constant over the range of length scales.

It remains to characterize onset of fracture at a site. In constructing a statistical theory the chance of fracture will be determined by a power law hazard function in the stress intensity of the form,

$$k(K) = \frac{m}{K_c} \left( \frac{K}{K_c} \right)^{m-1}. \quad (4)$$

The probability of fracture onset at a site will then be determined by a statistical function of the Weibull extreme value type. Onset of fracture will be statistically distributed about some critical stress intensity  $K_c$ .

Dynamic strength and the meso-kinetic features of the model come into play when stress loading rates exceed the rate at which the mesoscopic stress field can equilibrate over the correlation length scales. It is readily shown that the loading strain rate at this transition is on the order of  $\dot{\epsilon} \sim K_c / \rho_o c a_o^{n+1}$  where  $\rho_o$  and  $c$  are the material density and elastic wave speed, while  $a_o$  is the characteristic correlation length from Equation (3). Shock wave, or Heaviside, loading to an elastic stress state would stimulate nonequilibrium response of the mesoscale stress field. We will consider a shock wave crossing a material plane at time  $t = 0$  and develop a fracture activation hazard function as a function of time after passage of the shock wave. For much of the analysis, time will be considered in units of  $c^{-1}$ , where  $c$  is the elastic wave velocity, and use  $s = ct$  as the time measure. Of course  $s$  has a dimension of length. The temporal hazard function is calculated from,

$$g(s)ds = k(K)dK. \quad (5)$$

or ,

$$g(s) = k(K(s))K'(s). \quad (6)$$

During the time-dependent period of stress intensification about a fracture-producing defect, from Equation (2),

$$K(s) = \bar{\tau} s^n, \quad (7)$$

and,

$$K'(s) = n\bar{\tau} s^{n-1}. \quad (8)$$

Equations (4) through (8) lead to,

$$g(s) = mn \left( \frac{\bar{\tau}}{K_c} \right)^m s^{nm-1}. \quad (9)$$

Letting  $r = mn$  and the length scale  $\alpha_o = (K_c / \bar{\tau})^{1/n}$  yields for the temporal hazard function for fracture after passage of the shock wave,

$$g(s) = \frac{r}{\alpha_o} \left( \frac{s}{\alpha_o} \right)^{r-1}. \quad (10)$$

The Poisson distribution of correlation lengths associated with flaw sites implies the sites of size  $a < s$  will have achieved maximum stress intensification and, if not already activated, will no longer provide a site for fracture activation, and is removed from the population. Consequently, the hazard function in Equation (10) is modified by the exponential Poisson expression to provide,

$$h(s) = \frac{r}{\alpha_o} \left( \frac{s}{\alpha_o} \right)^{r-1} e^{-s/a_o}. \quad (11)$$

If the number of fracture sites in a volume element  $dV$  is  $N_o dV = dV / \lambda_o^3$ , where  $\lambda_o$  is the mean spacing, then the statistical rate of fracture activation per unit time, per unit volume, is,

$$n(s) = \frac{1}{\lambda_o^3} \frac{r}{\alpha_o} \left( \frac{s}{\alpha_o} \right)^{r-1} e^{-s/a_o}. \quad (12)$$

If the body of interest is an area or a line then the factor in Equation (12) is reduced to  $1/\lambda_o^2$ , or  $1/\lambda_o$ , to reflect the reduced dimensionality. Although it is not necessary, it seems reasonable that the nominal correlation length  $\alpha_o$  and average fracture site spacing  $\lambda_o$  would be comparable, and in the subsequent analysis  $\lambda_o = \alpha_o$  is assumed.

## Fracture Growth and Interaction

When fracture activate at appropriate sites the cracks rapidly accelerate to some characteristic velocity and propagate until arrested by some impediment to further crack propagation. In concert, the stress field driving the fracture is relieved as the crack propagates. This facet of the fracture process behind a shock wave has its own set of complicating factors. We will keep the modeling of fracture growth sensibly simple. Once activated crack acceleration to terminal velocity is governed by the same inertial properties that determine dynamic fracture activation [Freund, 1990]. Thus, it is sensible to fold the acceleration growth into the initial activation model and simply assume instantaneous acceleration to a terminal velocity. Both theoretical efforts and experimental observation show that terminal velocity for brittle cracks is some appreciable fraction of the elastic wave speed (proportional to the Rayleigh or shear elastic velocity for example). We will simply assume a constant crack growth velocity equal to  $c_g$ . Finally, if a fracture activates at an earlier normalized time  $\sigma = ct'$  and propagates to a later time  $s = ct$ , then a volume surrounding the crack of magnitude,

$$\nu(s - \sigma) = \frac{4\pi}{3} \eta^3 (s - \sigma)^3, \quad (13)$$

is assumed stress relieved, where  $\eta = c_g / c$  is the ratio of the crack growth velocity and the sound speed. Again, if the interest is fracture on an area, or a line, the power and coefficient in Equation (13) is modified accordingly.

## Analytic Framework for the Meso-Kinetic Failure Model

The essential physics that has been proposed to underlie the failure wave phenomena in brittle solids has now been addressed. This physics includes a mesoscopic stress field which overlays the continuum stress field impressed on the body in the shock compression process. Under rapid dynamic loading, such as in shock compression, this mesoscopic stress field does not instantaneously equilibrate, but does so over time as correlation length scales in the field equilibrated at elastic wave speeds. Fractures activate at sites of weakness as stress intensities increase to critical levels over time. Activated brittle fractures propagate at crack growth velocities and relieve the driving deviator stress field.

The objective now will be the development of an analytic framework based on this physics to describe response of the brittle material during fracture failure following a compressive shock wave. This will be accomplished by first identifying a parameter  $D(s)$ , which is the volume fraction of the solid over which shear stress has been relieved by the time-dependent fracture process at time  $s$ . It will be appropriate to identify  $D_x(s)$  as a fracture damage parameter. The integral,

$$D_x(s) = \int_0^s \nu(s - \sigma) n(\sigma) d\sigma, \quad (14)$$

provides the super position of the stress relieved volume from Equation (13) of all fractures activated at earlier time  $\sigma$  from Equation (12) integrated from the initial time zero up to the present time  $s$ .  $D_x(s)$  is identified as the extended damage, and is not the desired damage parameter since the integral is in error by not accounting for further activation of fractures in previously stress relieved regions (exclusion), nor does it account for the overlap of growing stress release regions (impingement) [Grady, 1981].

These features are accounted for through the statistical relation [Grady, 1981],

$$D = 1 - e^{-D_x}. \quad (15)$$

relating the extended damage parameter  $D_x$  to the damage parameter  $D$ . The damage  $D$  and the extended damage  $D_x$  are nearly equal at early time as they should be when fracture damage is still dilute. At late time  $D$  approaches unity whereas  $D_x$  is unbounded.

Replacing Equation (14) with the physical models for fracture activation and growth of stress release from Equations (12) and (13) yields,

$$D_x(s) = \int_0^s \frac{4\pi}{3} \eta^3 (s - \sigma)^3 \frac{r}{\alpha_o a_o^3} \left( \frac{\sigma}{\alpha_o} \right)^{r-1} e^{-\sigma/a_o} d\sigma. \quad (16)$$

Introducing the change of variables  $x = \sigma / \alpha_o$  and  $y = s / \alpha_o$  results in,

$$D_x = \frac{4\pi}{3} r \eta^3 \gamma^3 \int_0^y (y - x)^3 x^{r-1} e^{-\gamma x} dx, \quad (17)$$

where  $\gamma = \alpha_o / a_o$  is the dimensionless ratio of the two characteristic length parameters. The further transformation  $z = x / y$  reduces the equation to the convenient form,

$$D_x = \frac{4\pi}{3} \frac{r \eta^3}{\gamma^r} (\gamma y)^{r+3} \int_0^1 (1 - z)^3 z^{r-1} e^{-\gamma y z} dz, \quad (18)$$

Lastly, returning to the time dependence through  $\gamma y = s / a_o$ ,

$$D_x(s) = \frac{4\pi}{3} \frac{r \eta^3}{\gamma^r} (s / a_o)^{r+3} \int_0^1 (1 - z)^3 z^{r-1} e^{-(s/a_o)z} dz, \quad (19)$$

with  $D(s)$  provided by Equation (15).

The continuum shear stress  $\bar{\tau}(s)$  is then expected to be reduced for its initial value  $\bar{\tau}$  in response to the time-dependent growth of the damage  $D$ , either to zero, or to some reduced residual stress. A reasonable expression of this relaxation of the shear stress is,

$$\bar{\tau}(s) = \bar{\tau}(1 - D) + \bar{\tau}_r D. \quad (20)$$

The statistical number of activated fractures that participate in the failure process can now be calculated. The fracture number  $N(s)$  at time  $s$  is provided by the activation rate from Equation (12), but reduced by the current volume fraction of stress relieved material,

$$N(s) = \int_0^s (1 - D(\sigma)) n(\sigma) d\sigma = \int_0^s e^{-D_x(\sigma)} n(\sigma) d\sigma. \quad (21)$$

Equation (21) is not readily solvable because of the complexity of Equation (19) for  $D_x$ . The fracture number is easily estimated in most cases, however, as will be shown later.

## Application of the Meso-Kinetic Model

To explore the implications of the present meso-kinetic model, properties for soda-lime glass necessary for the model are developed. These properties are acquired through experience with the model, and are preliminary. They are sufficient, however, in reproducing some of the features observed in studies of failure waves in glass, and they provide a means for uncovering the behavior of the model under the dynamic mechanical stimulus of concern.

Table 1  
Meso-kinetic Model Properties for Soda-Lime Glass

Density	$\rho_o = 2500 \text{ kg/m}^3$
Sound Speed	$c = 5000 \text{ m/s}$
Fracture Speed	$c_g = 2000 \text{ m/s}$
Critical Stress Intensity	$K_c = 100 \text{ MPa m}^{1/3}$
Intensification Modulus	$n = 1/3$
Mesoscale Correlation Length	$a_o = 0.25 \text{ mm}$
Mesoscale Distribution Modulus	$m = 15$

Material and model parameters for soda-lime glass are provided in Table 1. An elastic sound speed of 5000 m/s is neither the longitudinal nor the shear wave speed, but rather a nominal value in between. At this juncture, the more appropriate wave speed is not known nor is it critical. A fracture speed of 2000 m/s is a reasonable guess at some value less than the sound speed. Note that the critical stress intensity does not have dimensions of fracture toughness. It is consistent with the present model generalization, where stress intensification is a consequence of both the defect structure and the neighboring mesoscopic correlation field. An intensification modulus of  $n = 1/3$  is a reasonable guess and determines the dimensions of  $K_c$ . A mesoscale correlation length of 0.25 mm was determined from several iterations of the model, as was the distribution modulus of  $m = 15$ .

The equations have been specialized to apply to a cross-section 10 mm in width and 1 mm in thickness, and providing the plots shown in Figure (6). Shock amplitude increases from left to right and is identified by the resolved shear stress behind the shock wave in each plot. Time dependence of the fracture number activated at each shock amplitude is shown in the three upper plots. The corresponding position and time of activation for one statistical complexion at each shock amplitude is illustrated in the lower plots. Damage growth occurs later in time as fracture growth and interaction proceeds. Reduction of the driving shear stress would correlate with the growth of fracture damage.

## Features of the Statistical Hazard Function

Equation (11) provides the statistical probability (hazard) function governing the likelihood that a potential fracture site will transition to an active fracture under the conditions imposed. This hazard function has unique features that are explored here in further detail. By letting

$S = s/a_o$  and  $\gamma = \alpha_o/a_o$  as before, Equation (11) transforms to a dimensionless hazard function.

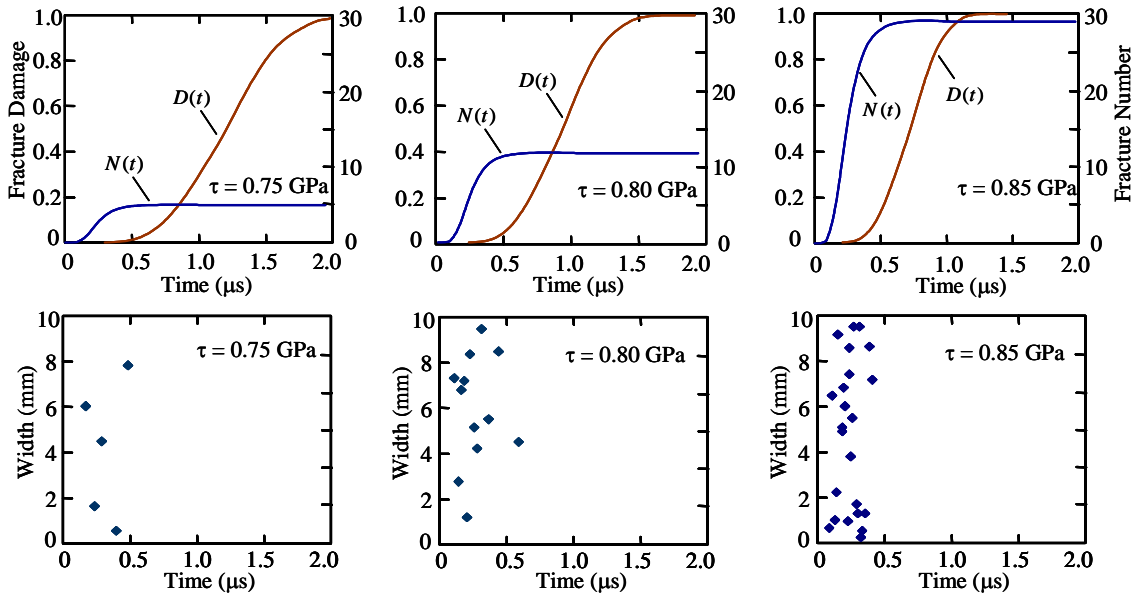


Figure 6: Representative application of the fracture kinetics model for soda-lime glass. Illustrates the statistical time dependent fracture activation and damage growth following passage of a shock wave. Increasing shock intensity is noted by the shear stress amplitude.

The hazard function,

$$H(S) = \frac{r}{\gamma^r} S^{r-1} e^{-S} \quad (22)$$

is the product of two terms. The first power function determines the increasing time-dependent chance that the defect will achieve critical stress intensification and activate fracture. The second exponential term determines the chance that the site will achieve stress equilibrium and drop out of the population of potential fracture flaws.

The hazard function is governed by the two dimensionless parameters  $r$  and  $\gamma$ . The parameter  $r$  is the product  $r = mn$ . The parameter  $m$  determines the spread in critical stress intensity at which a defect activates. As  $m$  is increased the spread narrows and trends toward conditions where all defects activate at the same critical stress intensity. The parameter  $n$  determines the time-dependent rate of stress intensification and it is argued that the combined intensification effect of both the defect and the neighboring correlation field is to reduce  $n$  to values less than the Griffith singularity of  $n = 1/2$ . Since  $K(s) \sim s^n$  the rate of growth is  $\dot{K} \sim ns^{n-1}$ , or  $\dot{K} \sim n$  as  $s$  approaches unity. The effect of decreasing  $n$  is to

increase the spread in fracture activation. For the parameters selected for soda-lime glass in Table 1  $m=15$  and  $n=1/3$  leads to  $r=5$ .

The parameter  $\gamma$  is the ratio of the two length scales  $\alpha_o$  and  $a_o$ . The length scale  $a_o$  is a material property characterizing the nominal long-range correlation within the mesoscopic stress field. The length scale  $\alpha_o = (K_c / \bar{\tau})^{1/n}$ , on the other hand, is a function of the global stress field and determines the length scale above which the stress  $\bar{\tau}$  is sufficient to cause fracture activation.

Together  $r$  and  $\gamma$ , through the function  $H(S)$ , determine the character of the fracture activation process. For a large collection of fracture sites,  $H(S)$  provides the statistical rate of fracture activation. For a single site the cumulative probability of fracture activation is provided by,

$$P(S) = 1 - e^{-\int_0^S H(\sigma) d\sigma}. \quad (23)$$

The exponent,

$$\frac{r}{\gamma^r} \int_0^S \sigma^{r-1} e^{-\sigma} d\sigma, \quad (24)$$

includes the complementary incomplete Euler gamma function  $\Gamma_c(r, S)$  and Equation (23) can be written,

$$P(S) = 1 - e^{-\frac{r}{\gamma^r} \Gamma_c(r, S)}. \quad (25)$$

In the limit of large  $S$  Equation (25) reduces to,

$$P(\infty) = P_\infty(\gamma) = 1 - e^{-\frac{r}{\gamma^r} \Gamma(r)} = 1 - e^{-\frac{r!}{\gamma^r}}, \quad (26)$$

where  $\Gamma(r)$  is the Euler gamma function and the final expression with the factorial term applies when  $r$  is an integer.  $P_\infty(\gamma)$  provides the probability that a single site will activate under the specified conditions.

The character of the fracture activation hazard function is illustrated in Figure (7). Properties from Table 1 are used, and a stress of  $\bar{\tau} = 0.9$  GPa is assumed, providing a value of  $\gamma \approx 5.5$ . The plot shows both the power law activation and exponential depletion terms separately, in addition to the complete

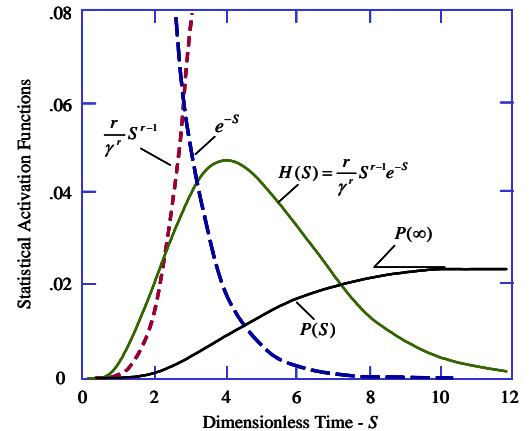


Figure 7: Construction of the fracture activation hazard function including power law activation and exponential depletion.



hazard function and the corresponding cumulative probability fracture function. For the selected stress amplitude, a fracture site has an approximately 2% probability of fracture ( $P_{\infty}(5.5) \approx 0.023$ ) and will occur within a time duration of about  $1 < S < 10$ .

As the driving stress amplitude is raised (decreasing  $\gamma$ ) the likelihood that a potential fracture site will activate increases and rapidly approach unity. This transition to unit cumulative probability is readily quantified by equating the relevant argument in the exponent of Equation (26) to one, or,

$$\frac{r!}{\gamma^r} = 1. \quad (27)$$

The transition curve in the hazard-function parameter space identifying the domain in which fracture activation is sparse is identified in the left plot of Figure (8). The right plot shows an alternative representation of the fractional activation probability for selected values of  $r$ .

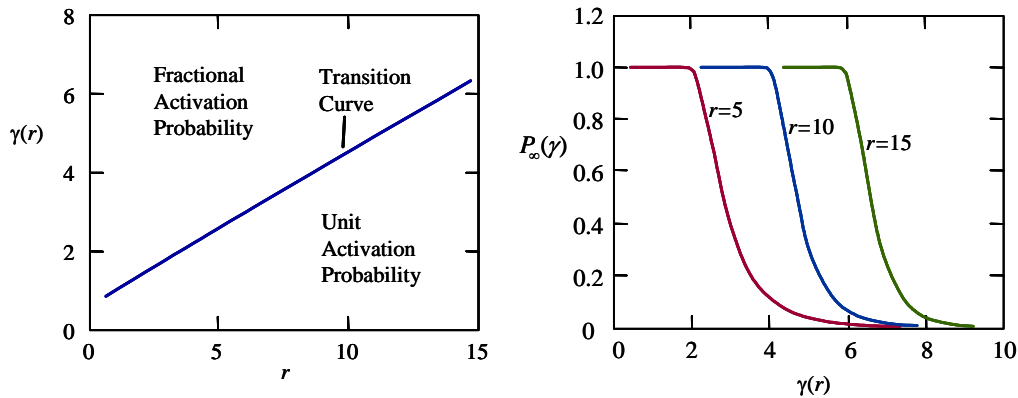


Figure 8: Parameter plots of fracture activation hazard function identifying domain of sparse or fractional fracture activation.

## Model Featured Requiring Further Development

The physics emphasized in the present fracture model is the time delay necessary to the equilibration of elastic stress throughout the heterogeneous mesostructure following passage of a rapidly rising shock wave. The statistical model within which this physics has been incorporated readily predicts the delayed fracture (the failure wave) observed in the shock-induced failure of brittle materials. The model predicts a dependence of the failure delay on the shock amplitude. The model does not predict a separate and different velocity for the failure wave as reported in several of the experimental studies; although this observation is still being debated. In any case this lack of the model may be a consequence of the overly simplistic damage growth model. A growth model that is dependent not only on the driving stress but also on the current damage in the neighborhood of failure may introduce a distinct failure wave velocity. These additional features of the model are being pursued.

Stress intensification with power-law dependence has the appearance of being a step backwards. Square root singularity associated with Griffith flaws has become common lore. Nonetheless, the more complex characterization may be necessary, although this must be examined in more detail.

## *Relationship of Physics Based Model to Other Studies*

Some relationship has been noted of the present model with recent research at Rutgers University [Niesz, 2005], and computational model development and validation [Holmquist and Johnson, 2006]. Some observations on these connections are documented in this subsection.

### **Defect Studies in Armor Ceramics**

Efforts are underway Rutgers University to assess the nature of defects in armor quality silicon carbide ceramic [Niesz, 2005]. In the framework of the present meso-kinetic model of dynamic failure in brittle solids, the strength and length scale of a failure-producing defect is determined by its local mechanical stress-strain response. Consequently, the effective length scale of a defect identified through this mechanical characterization is not necessarily expected to correspond to a geometric defect length scale determined through some material micro-imaged technique. Never-the-less, some correlation of defect geometric size and model meso-kinetic length scale would be expected. Efforts at Rutgers University are determining, through field emission scanning electron microscopy, populations and geometric length scales associated with carbon defects in silicon carbide ceramic. Although not directly pertaining to the physics-based gamma distribution found to describe dynamics of the failure process in the present meso-kinetic model, use of an inverse gamma function to describe the geometric population is interesting. Defects tend to peak in the 20 to 30  $\mu\text{m}$  range. Of particular importance, however, is the population of larger defects in the power law tail of the distribution and the fact that this population differs in the two different materials that were examined.

### **The JHB Model and Relationships to the Present Theory of Strength and Failure**

The word “fail” as used in the terms “material failure”, or “failed material”, or “strength of failed material” lies at the heart of the respective modeling efforts. The word, and the terms in which it is used, commonly do not have the same meaning throughout the mechanics and physics community concerned with the strength of solids under shock and high-rate loading. This disparity can be disconcerting. Hence, care in the various definitions is warranted.

Under sufficiently large amplitude uniaxial strain shock compression all materials, including the high strength ceramics of current interest, achieve an elastic limit above which irreversible inelastic deformation proceeds. Although this elastic limit (the Hugoniot elastic limit, or HEL) is sometimes referred to as failure under shock compression; this is precisely not the definition in the JHB model development [Holmquist and Johnson, 2006]. It is

perhaps more appropriate, in analogy with the behavior of metals under shock compression, to identify this elastic limit as yielding even though the underlying mechanisms may, or may not, be the same. Yielding of ceramics under strong shock compression is the onset of inelastic deformation that limits the subsequent increase in the shear (or deviator) stress of the material. If the shear stress under subsequent deformation remains either sensibly constant, or increases as a result of continued deformation hardening, then the ceramic is regarded as having yielded under shock compression but not failed. Failure of the ceramic is considered to occur if the deformation processes subsequent to yield leads to a marked reduction of the shear stress and a softening of the strength of the material. Strength is the maximum shear stress the material can support under the stated loading conditions. Strength and shear stress are quantitatively the same when the inelastic deformation is in process.

Failure and the concomitant reduction in the shear stress and material strength in ceramics in the shock event are assumed a consequence of a process of fine-scale microfracture. The fracture occurs over a finite inelastic strain and reduces the strength of the ceramic from that of the intact ceramic (either the initial yield strength or the subsequent strength at onset of failure) to that of a fine-grained powder of the ceramic at the requisite confining pressure and strain rate. Because of the fine particle size the process has been referred to, perhaps inappropriately, as one of comminution in analogy with the mechanical processes used to reduce ceramic materials to powders and grits of the same material. Fragmentation in the dynamic fragmentation event is addressed in a later section.

Failure in the shock event through dynamic fracture is a reasonable assumption. Other methods of testing the strength of high-strength ceramics reveal catastrophic fracture to be the dominant failure mechanism. It is recognized, however, that the shock compression event may be unique. Failure through mechanisms other than dynamic microfracture are possible. A leading alternative mechanism that has been proposed for the failure of ceramics under shock compression is that of localized thermoplastic deformation. Deformation-induced adiabatic heating on an inhomogeneous network of thin shearing planes can lead to shear stress reduction and accommodation of the inelastic deformation.

How this thermoplastic failure mechanism would modify the current constitutive model for ceramics has not yet been explored. Certain differences are evident, however. For example, bulking is a natural consequence of the dynamic fracture failure process and the transfer of elastic shear strain energy to energy of volumetric strain is a necessary step in the modeling. The same elastic shear strain energy would transition to localized thermoplastic heating under a mechanism of failure through inhomogeneous thermoplastic shear negating the need for a bulking term in the constitutive model.

It is reasonable to suspect that a specific ceramic could exhibit failure through both microfracture and localized thermoplasticity; perhaps transitioning from the former to the latter under increasing shock intensity as both rates of deformation and confining pressure become increasingly more intense.

## IV Impact Breach of Glass and Ceramic Plate

The breach of a glass or ceramic plate by the impact of a comparable dimension chunky projectile provides a particularly challenging problem to computational solution methods. The reasons for this are several: Experimental results indicate that properties of the plate material governing the strength and the resistance to breach are nonlocal and time dependent. This behavior provides an immediate handicap to computational solutions based on local, time independent strength and failure models. Further, the impact conditions at onset of breach are statistical providing additional complexity to a deterministic calculation of breach.

In the present section an analytic physics-based model of the onset of breach of plates of brittle material is pursued. The model has application, for example, to the high-speed impact of solid fragments on transparent shielding such as high strength glass or possibly brittle polymeric material such as Plexiglas polymethyl (methacrylate) or Lexan (polycarbonate). The model would be equally applicable to fragment or bullet impact on barriers of ceramic plate. Emphasis of the model is at impact conditions near the threshold of breach of the barrier.

This effort was initiated in an earlier report [Grady, 2005]. The present study modifies and extends the earlier development. Additionally, recent data on the impact of steel spheres with plates of float glass [Sun *et al.*, 2006] nicely delineates the breach threshold. These data, when joined with the analytic model, clearly emphasis the time-dependent strength and failure features that must be captured with a successful computational model.

The purposes of the present analytic modeling effort are several. First, as just stated, one purpose is to clearly illustrate through the analytic model the time-dependent properties of brittle material that must be captured in a computational model of the breach phenomena. A time-dependent Tuler-Butcher failure criterion [Tuler and Butcher, 1968] is joined with the analytic model to provide a breach criterion for projectile impact on glass plate. Further, the analytic model reveals geometric and material scaling rules appropriate to the breach event and identifies further constraints to a computational solution. Understanding of the scaling characteristics of the impact event also enhances understanding of the underlying terminal ballistics physics. Lastly, analytic solutions can lead to useful engineering models that have had, and will continue to have, practical application.

### *The Ballistic Model*

The ballistic event and the details of the physical model are illustrated in Figure (9). A chunky projectile (fragment) of characteristic size  $a$  (a sphere is a reasonable idealization but not necessary) is incident on a plate of thickness  $b$  with normal velocity  $V$ . The velocity vector need not be normal to the barrier plate although the model is not appropriate for large angles of obliquity.

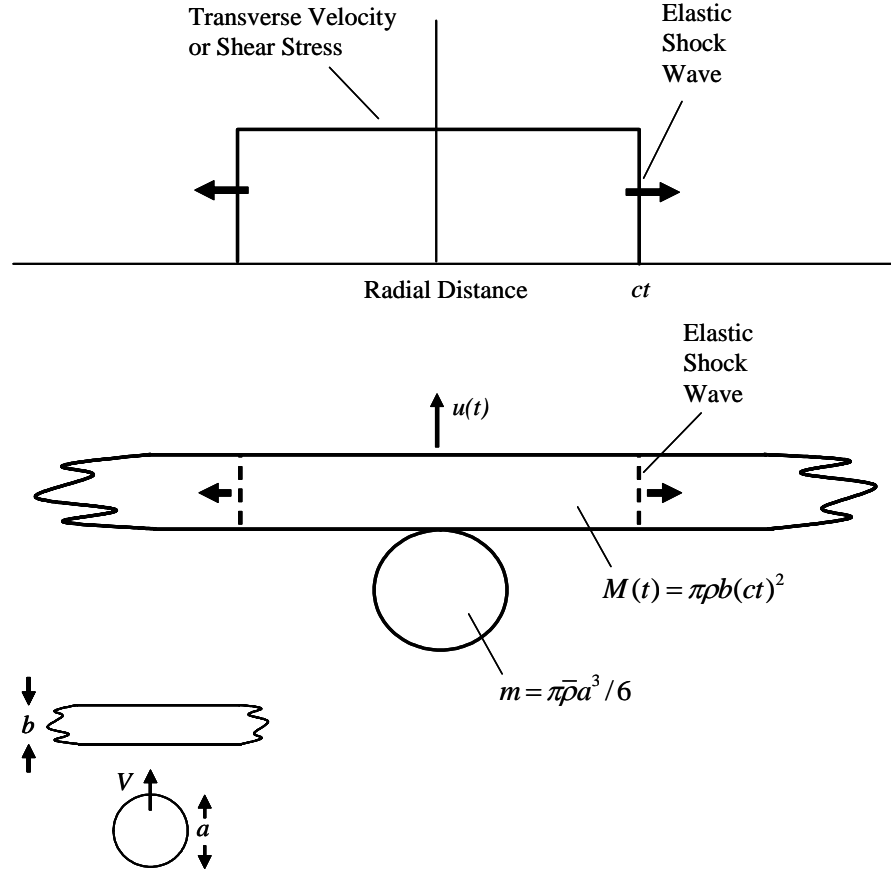


Figure 9: Model of a fragment impact on a brittle solid barrier; Inset illustrates size scales and initial relative motion. Drawing and graph shows the motion and participating masses at time  $t$  of the projectile and disc portion of plate of current radius  $ct$

Transfer of momentum and energy occurs through a radial elastic transverse shock wave. Elastic stress waves within the projectile and plate mass encompassed by the shock wave are ignored and the material is all assume to be at the same momentum-averaged axial velocity  $u(t)$ . The projectile deceleration is calculated through a momentum balance between the projectile and the mass of the plate encompassed by the outwardly directed shock wave. The mass of the plate increases with time after impact according to  $M(t) = \pi \rho b (ct)^2$  where  $M$  is the mass of the region,  $\rho$  is the plate density,  $b$  is the plate thickness and  $c$  is the elastic shear wave velocity of the plate material. If  $m$  is the mass of the projectile then momentum conservation requires,

$$d(m + M)u = (m + M)du + u dM = 0, \quad (28)$$

where  $u(t)$  is the time dependent velocity of the projectile and plate mass  $M(t)$  as illustrated in Figure (9). Equation (28) integrates to,

$$u = \frac{V}{1 + M/m}. \quad (29)$$

By introducing the plate and projectile masses,

$$M = \pi \rho b (ct)^2, \quad m = \pi \bar{\rho} a^3 / 6, \quad (30)$$

Equation (29) is rewritten in the explicit time dependent form,

$$u = \frac{V}{1 + (t/\tau)^2}. \quad (31)$$

The time constant,

$$\tau = \sqrt{\frac{m}{\pi \rho c^2 b}} = \sqrt{\frac{1}{6} \frac{\bar{\rho}}{\rho} \frac{a^3}{c^2 b}}, \quad (32)$$

is identified as a characteristic load transfer time that is dependent on both the geometry and the properties of the plate and projectile material.

The decelerating force on the projectile is calculated from  $F = -m du/dt$  and using  $u(t)$  from Equation (31),

$$F = \hat{F} \frac{t/\tau}{(1 + (t/\tau)^2)^2}, \quad (33)$$

with,

$$\hat{F} = \frac{2m}{\tau} V = \left( \sqrt{\frac{2\pi^2}{3} \bar{\rho} \rho a^3 c^2 b} \right) V. \quad (34)$$

The time dependence of the decelerating force is shown in Figure (10). A maximum force is achieved at  $t/\tau = 1/\sqrt{3}$  with amplitude  $F/\hat{F} = \sqrt{27}/16 \approx 1/3$ .

The opposing shear stress  $T(t)$  in the glass plate is calculated from the shock jump condition across the elastic shock wave,

$$T(t) = \rho c u(t). \quad (35)$$

From Equation (31) this relation for the shear stress becomes,

$$T(t) = \hat{T} \frac{1}{1 + (t/\tau)^2}, \quad (36)$$

where,

$$\hat{T} = \rho c V. \quad (37)$$

The time dependence of the opposing shear stress in the plate is also shown in Figure (10). The latter calculation of the shear stress differs from the previous years approach and is regarded as an improvement in the model.

An interesting alternative calculation of the shear stress follows from energy considerations. Since momentum is conserved in the model kinetic energy is not. The difference in kinetic energy of the plate and projectile at any time can be ascribed to strain energy in the plate. The elastic expression for strain energy results in the same measure of shear stress provided by the shock jump in Equation (36).

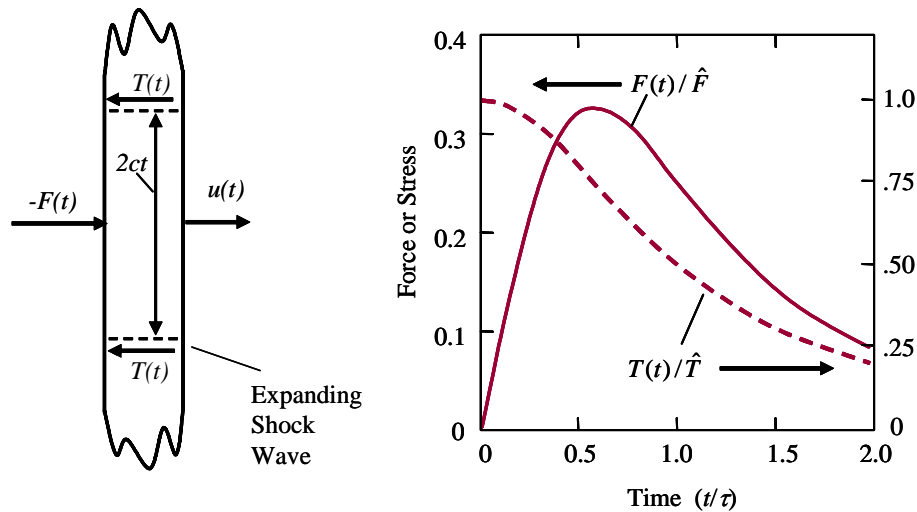


Figure 10: The decelerating force  $F(t)$  and the opposing shear stress  $T(t)$  in the responding portion of the barrier plate. Ordinates for  $F(t)$  are on the left and for  $T(t)$  on the right

Several assumptions are tacit in the present model. In the model the several energy transfer processes that occur in the motions and deformations leading to arrest of the projectile or failure of the barrier plate are decoupled. Kinetic energy of the incident projectile is assumed to transfer to kinetic energy of the impeding plate, and that this kinetic energy in turn converts to elastic strain energy of the plate. The latter strain energy is not explicitly calculated or used in the analysis, however, and is only inferred from the shear stress state. Rigidity of the plate mass encompassed by the shock wave as implied by the uniform velocity  $u(t)$  is certainly not correct. Marked spatial variations in this velocity as the elastic wave propagates outward from the point of impact would occur. The momentum averaged velocity  $u(t)$ , and corresponding shear stress, arising from the present model adequately characterizes the dynamics necessary for the prediction of failure in the present application. Failure occurs when and if some criterion resulting from this dynamics is exceeded during the process. This assumption is reasonable as we are here solely concerned with threshold

conditions and are using the model to determine sensible functional forms for the limiting velocity at failure and the dependence on parameters of the problem.

## Failure Criterion

A failure criterion appropriate to the impact event will now be developed. The choice here will be the Tuler-Butcher failure criterion [Tuler and Butcher, 1968] based on the time dependent shear stress caused by the impact and stated in the form,

$$I_n(t) = \int_0^t \left( \frac{T(t)}{\rho c} \right)^n dt \leq K_n . \quad (38)$$

Survival of the barrier is assured while the Tuler-Butcher integral  $I_n(t)$  remains less than the material constant  $K_n$ . The barrier is breached when  $K_n$  is exceeded. Normalizing the stress by  $\rho c$  is not necessary but is done here to simplify the expressions. In this form the integral has dimensions of velocity to the power  $n$  multiplied by time.

This criterion is found to be quite general, and actually covers several specific criteria of particular interest. The parameter  $n$  in the Tuler-Butcher criterion can range from about one to quite large, and the range  $1 \leq n < \infty$  is considered. Within this range a failure criterion governed by a critical impulse, a critical energy or a critical stress is spanned. The present Tuler-Butcher failure criterion coupled with the present model will also bring to light scale dependent issues observed in experiments as well as some of the complicating issues for computational simulation of the brittle failure on impact.

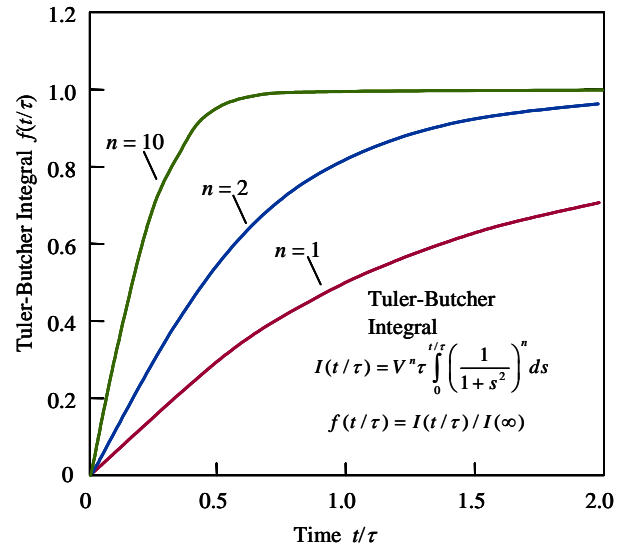


Figure 11: Time dependence of the Tuler-Butcher integral for breaching a glass barrier for selected values of  $n$ .

Introducing the expression for  $T(t)$  from Equation (36), the criterion can be written,

$$I(t/\tau) = V^n \tau \int_0^{t/\tau} \left( \frac{1}{1+s^2} \right)^n ds \leq K_n . \quad (39)$$

The barrier is breached according to the present Tuler-Butcher criterion when the time dependent integral on the left exceeds  $K_n$ . Let the function  $f(t/\tau) = I(t/\tau) / I(\infty)$ . Time dependence of the integral is illustrated in Figure (11) for  $n = 1, 2$  and  $10$ . Growth of the



Tuler-Butcher integral is slowest for  $n = 1$  (impulse criterion), more prompt for  $n = 2$  (energy criterion) and most rapid for  $n = 10$  (approaching a constant stress criterion).

The barrier is not breached if, as time becomes large corresponding to  $f(t/\tau) \rightarrow 1$ ,

$$\beta_n V^n \tau \leq K_n, \quad (40)$$

Where,

$$\beta_n = \int_0^\infty \left( \frac{1}{1+s^2} \right)^n ds \quad (41)$$

is the integral expression in Equation (39) in the limit of large time. The integral in the Tuler-Butcher expression is analytic and equal to,

$$\text{atan}(t/\tau), \quad (42)$$

for  $n = 1$ ,

$$\frac{1}{2} \left( \frac{t/\tau}{1+(t/\tau)^2} + \text{atan}(t/\tau) \right), \quad (43)$$

for  $n = 2$ ,

and successively more complex functions of the inverse tangent for higher values of  $n$ . For Equation (41) these relations provide  $\beta_1 = \pi/2$  and  $\beta_2 = \pi/4$ .

The characteristic load-transfer time constant  $\tau$  from Equation (32) is written,

$$\tau = \frac{a}{c} \sqrt{\frac{1}{6} \frac{\bar{\rho} a}{\rho b}} = \frac{a}{c} R. \quad (44)$$

The parameter  $R$  is dimensionless and is constant when replica scaling is applied to the system (the projectile dimension  $a$  and the barrier thickness  $b$  are proportionally changed). Equation (40) is plotted as an equality for the selected values of  $n$  in Figure (12) with  $K_n/\beta_n = 1$ . The time constant  $\tau$  scales directly with the size  $a$  of the projectile, and hence, the system size under replica scaling.

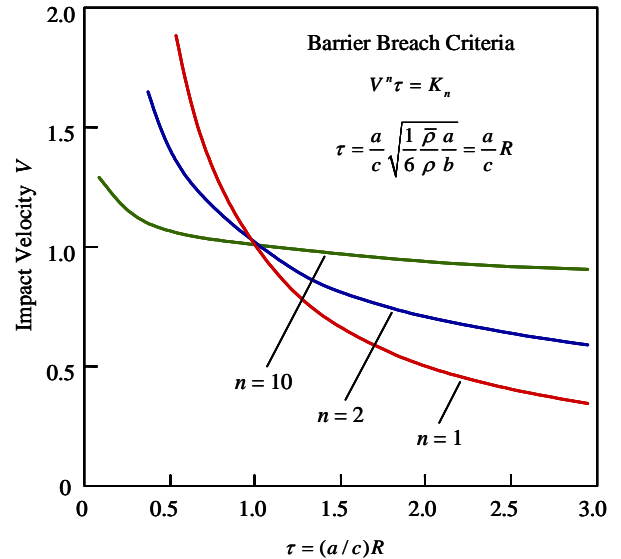


Figure 12: Barrier breach criteria for selected values of the Tuler-Butcher parameter  $n$ .

Increasing values on the abscissa, maintaining  $R$  constant, implies increasingly larger replica scaled projectile-barrier systems. The threshold velocity for onset of breach decreases with the system size for each of the three cases shown in Figure (12). Scale dependence is most pronounced for the Tuler-Butcher impulse criterion ( $n=1$ ), less so for the energy criterion ( $n=2$ ), and approaches independence of system scale for large  $n$  (approaching a failure stress criterion).

## Experiments on Impact Breach of Float Glass

Recent studies in which steel ball bearings impact plates of soda-lime glass [Sun, *et al.*, 2006] provide appropriate data for exploring the model developed in the present impact breach study. In the tests steel spheres are accelerated to velocities ranging over about 15 to 25 m/s and caused to undergo normal impact on glass plates. Steel spheres were either 1/4 in. (6.350 mm) or 3/8 in. (9.525 mm) diameter. Barrier plates were either 1.6 mm or 2.3 mm in thickness. The reported criterion for breach of the glass plates was that they were either broken or unbroken.

The data of Sun *et al.* (2006) are replotted from their report in Figure (13). The ordinate is the impact velocity. On the abscissa is the characteristic load transfer time provided by Equation (32) or Equation (44). A density of 7840 kg/m<sup>3</sup> is used for the steel. A density of 2530 kg/m<sup>3</sup> and shear wave speed of 3.47 km/s are used for the soda-lime glass. Solid symbols identify the broken (breached) glass plates. Open symbols are for the unbroken plates. The breach and no-breach symbols at each impact condition are offset slightly in the figure for easier visualization.

Tuler-Butcher failure criteria for  $n = 1, 2$ , and 3 are independently compared with the data. Of the three the data appear best described with an  $n = 2$ , or an energy-based, Tuler-Butcher criterion although the significant scatter introduces some uncertainty to this observation. Particularly important is the lack of replica scaling of the breach strength data as shown by the two intermediate sets of data provided in Figure (13).

The same data are replotted in Figure (14) against the replica scale parameter  $R$  showing the near replica scaling of the test with 6.35 mm steel spheres on 1.6 mm glass plates and the 9.35 mm spheres on 2.3 mm plates.

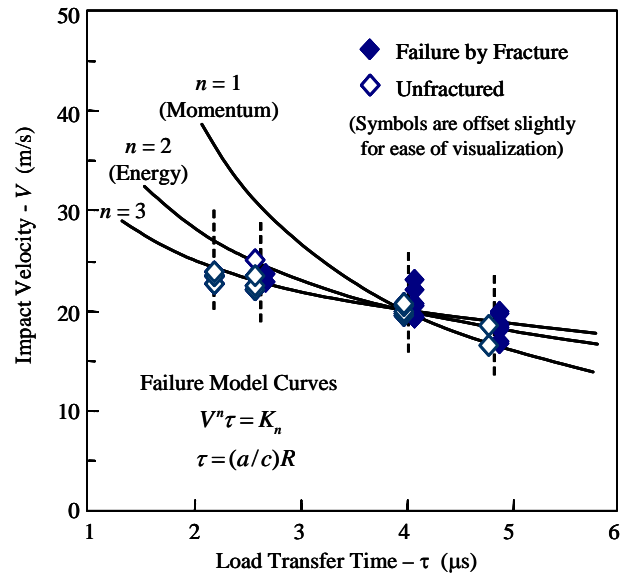


Figure 13: Breach data for steel sphere on glass plate experiments [Sun, *et al.*, 2006]. Comparison with selected Tuler-Butcher criteria.

The replica scale parameter for the two differ by less than 6% whereas system size differs by about 50%. Note also that the smaller scale test exhibits statistically higher breach strength.

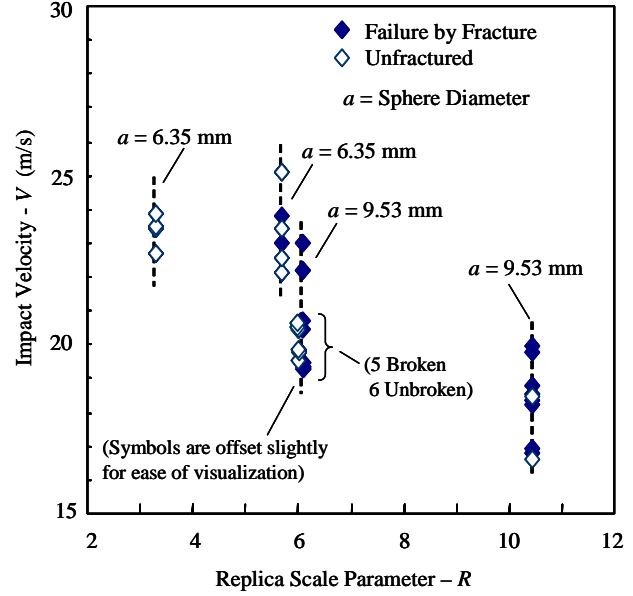


Figure 14: Breach data for steel sphere on glass plate experiments [Sun, et al., 2006]. Abcissa is the replica scale parameter and is proportional to the ratio of the sphere diameter to plate thickness.

## Failure Toughness of Glass Plate

Working with the impact breach data of Sun *et al.* (2006) and the Tuler-Butcher failure criterion, the data support an energy-based or  $n=2$  Tuler-Butcher failure criterion. Although no theoretical work has demonstrated that this energy-based response need be, there is a history of evidence that support dynamic failure of brittle solids described by some form of an energy criterion.

For the present data on soda-lime glass an energy-based Tuler-Butcher criterion best describes the breach data as illustrated in Figure (13). The value of  $K_2$  determined from the fit to the data is  $K_2 = 1.26 \times 10^{-3} \text{ m}^2\text{s}$ . Failure energy is calculated through,

$$\Gamma_f = \rho c K_2. \quad (45)$$

Using the density  $\rho$  and the shear wave speed  $c$  for soda-lime glass in the previous relation, a value of  $\Gamma_f = 11.0 \text{ MJ/m}^2$  is obtained. A property  $K_f$  will be identified through the relation,

$$K_f = \sqrt{2\rho c^2 \Gamma_f}, \quad (46)$$

if for no other reason than numerical comparison with the known fracture toughness of glass. The property  $K_f$  will be called the failure toughness of the glass plate. The Tuler-Butcher

toughness may also be an appropriate naming. Carrying through the calculation yields a value of  $K_f = 25.9 \text{ MPa m}^{1/2}$ . Note that the failure toughness is markedly larger than the nominal fracture toughness for soda-lime glass which is of order  $K_c \approx 0.5 - 1.0 \text{ MPa m}^{1/2}$ .

The present failure toughness is not an intrinsic property of the glass but may provide a sensible property characteristic of impact failure of the glass plate. This strength property depends not only on the intrinsic strength of the glass but also on the flaw structure of the surface and interior of the plate. Further discussion on this issue will follow the next subsection addressing fracture damage resulting from breach of the glass plate.

## Post-Failure Fracture Damage

Failure of the glass plate upon impact based on the present model is achieved when the Tuler-Butcher integral exceeds the critical value. From the data of Sun *et al.* (2006), failure of the present soda-lime glass plate is best described by a Tuler-Butcher energy criterion ( $n = 2$ ) with a critical value of  $K_2 = 1.26 \times 10^{-3} \text{ m}^2 \text{ s}$ .

Post-failure fracture damage can be estimated with an extension of the present model. An estimate is provided for the extent and the density of cracking resulting from the local impact as well as the residual velocity of the impacting projectile and leading fragment debris. The model may have some validity to perhaps a few times the velocity at onset of failure. It is not intended as a predictive engineering model but rather a study with the intent of enlightening the physics of the plate impact failure and fragmentation process. With some additional effort, however, a fairly credible engineering model could perhaps emerge from the analysis.

In developing the model we will work with the 3/8" steel sphere impact on 2.3 mm glass plates [Sun *et al.* (2006)] for which the failure threshold velocity is approximately 20 m/s as is readily seen from Figure (13) or calculated from the Tuler-Butcher criterion with the critical  $K_2 = 1.26 \times 10^{-3} \text{ m}^2 \text{ s}$  derived previously. The characteristic time constant from Equation (32) for this problem parameters is  $\tau = 4 \times 10^{-6} \text{ s}$ . The Tuler-Butcher energy integral from Equations (39) or (43) is plotted in Figure (15) for selected velocities in excess of the failure threshold velocity. The time to failure  $t_f$  is calculated for each case in units of  $\tau$  and is  $t_f = 1.41, 0.623, 0.382$  and  $0.202$  times the constant  $\tau$  for impact velocities of  $V = 21, 25, 30$  and  $40 \text{ m/s}$ , respectively.

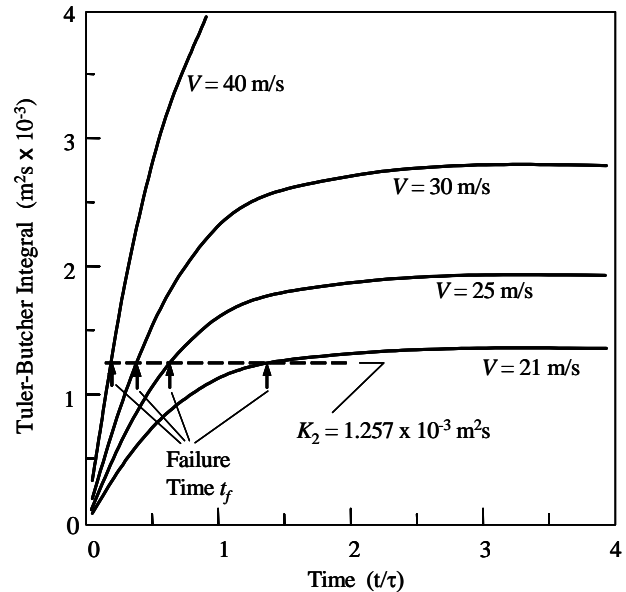


Figure 15: Tuler-Butcher energy integrals for impact velocities in excess of the threshold failure velocity.

Post-failure fracture damage is estimated by calculating the characteristic fracture spacing at a radius  $r$  from the point of impact. An estimate of the circumferential fracture spacing is provided through a balance of the resisting fracture energy  $\Gamma$  and the driving expansion kinetic energy. This analysis provides the following relation for the number of fractures generated by the impact that survives at a radius  $r$ ,

$$N(r) = 2\pi \sqrt[3]{\frac{\rho V^2}{48\Gamma}} r^{1/3} \left( 1 + \frac{1}{\tau^2} (t_f + r/c_g)^2 \right)^{-2/3}. \quad (47)$$

Fracture number from Equation (47) for the selected impact velocities is shown in Figure (16). A fracture resistance energy of  $\Gamma = 16.4 \text{ J/m}^2$  is used in Equation (47) based on a fracture toughness for glass of  $1 \text{ MPa m}^{1/2}$  and the expression for  $\Gamma = K_c^2 / 2\rho c_g^2$ . The elastic shear wave speed for glass is assumed for the fracture growth velocity  $c_g$  in Equation (47). The increased fracture intensity with increasing post-failure impact velocity is sensible but no data have been found to test the predicted trend. It is worth noting that at large range the fracture intensity dependence on range becomes power law (fractal) with an  $N(r) \sim 1/r$  dependence.

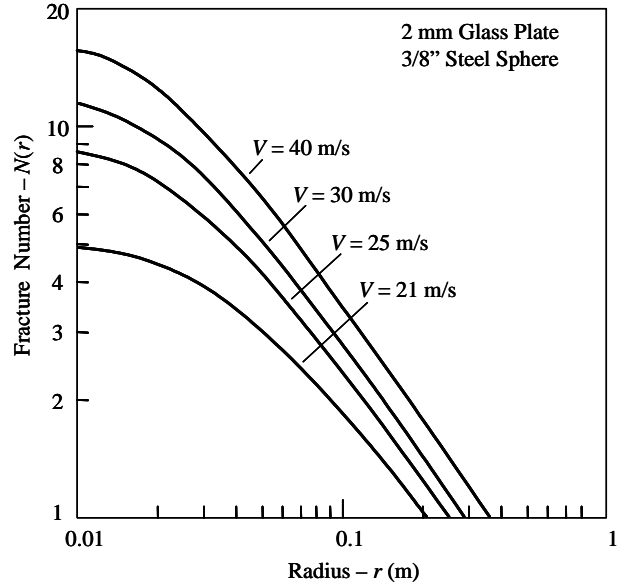


Figure 16: Fracture number dependence on the radial distance from impact point for steel sphere impact on glass plate.

A pictorial representation of the same fracture data is illustrated in Figure (17). Fractures are distributed at random on the circumference through a Voronoi statistic process [e.g., Grady, 2006].

The impact fracture damage relation in Equation (47) is developed through the following arguments. At any radius  $r$  the average circumferential spacing  $L$  of fractures is determined from the energy based fragment size relation [Grady, 1988],

$$L = \left( 48\Gamma / \rho \dot{\epsilon}^2 \right)^{1/3}, \quad (48)$$

yielding the fracture number at the radius  $r$ ,

$$N(r) = 2\pi r / L = 2\pi r \left( \frac{\rho \dot{\epsilon}^2}{48\Gamma} \right)^{1/3}. \quad (49)$$

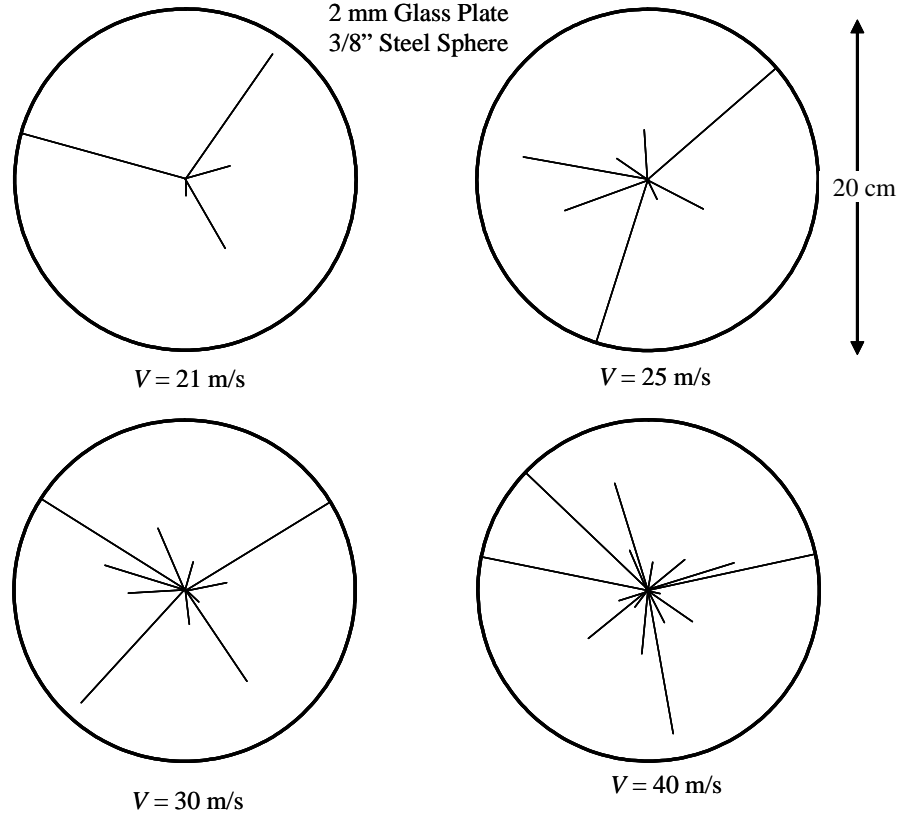


Figure 17: Post-impact fracture damage to glass plate. Velocities are successively higher than the critical breach velocity of 20 m/s.

The circumferential strain rate at  $r$  is provided by,

$$\dot{\epsilon} = \frac{u(r)}{r} = \frac{V}{r} \frac{1}{1 + (t/\tau)^2}, \quad (50)$$

where the velocity  $u(r)$  from Equation (31) is introduced. Equations (49) and (50) combine to give,

$$N(r) = 2\pi \sqrt[3]{\frac{\rho V^2}{48\Gamma}} r^{1/3} \left( \frac{r}{(1 + (t/\tau)^2)^2} \right)^{1/3}. \quad (51)$$

A constant fracture growth velocity  $c_g$  is assumed such that  $r = c_g(t - t_f)$  provides the radius of the fracture system at time  $t$  and is used to eliminate time from Equation (51) providing the fracture damage relation in Equation (47).

## Residual Projectile Velocity

The post-failure residual velocity of the projectile (and the leading fragment debris if a more sophisticated fragmentation model was employed) can be calculated from the model. As noted previously, the time  $t_f$  at which the Tuler-Butcher failure criterion is exceeded and failure (breach) of the plate achieved can be calculated for any impact velocity. Time to failure for selected impact velocities are shown in Figure (15). The velocity of the projectile at time  $t_f$ , and hence the residual projectile velocity is provided by,

$$u_f = \frac{V}{1 + (t_f / \tau)^2} . \quad (52)$$

A residual projectile velocity plot compared with the impact projectile velocity provided by the model is shown in Figure (18). The selected impact velocity amplitude, and the projectile and plate dimensions, are the same as for the fracture damage calculation.

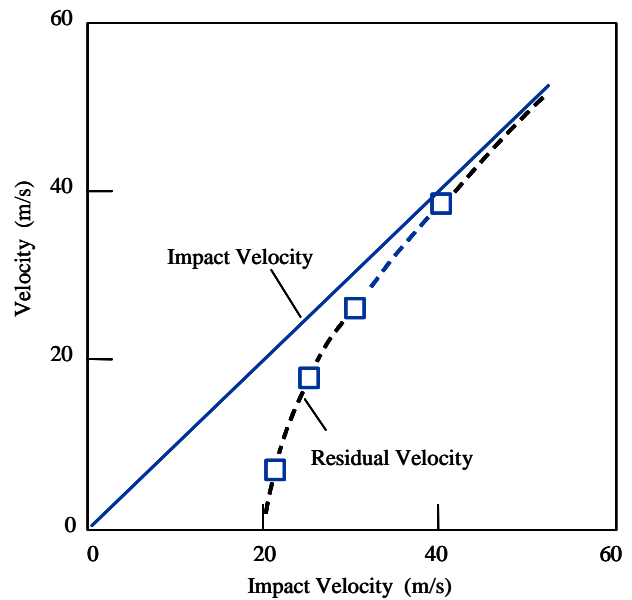


Figure 18: Residual velocity of projectile and leading fragment debris at selected velocities.

## V Fragmentation of Ceramics

Failure of ceramic in the ballistic event involves pervasive brittle fracture and fragmentation of the high-strength material. Ballistic resistance of ceramic involves the strength up to failure, and the continued strength through and beyond the fracture and fragmentation stages of the response. Physics-based modeling of the ceramic response for purposes of predicting ballistic events requires physical understanding of the nature of the dynamic fracture and fragmentation behavior of the brittle solids. Efforts in the present section continue to build on the physics of fracture and fragmentation of brittle solids in the ballistic event.

The statistical features of brittle fracture have been pursued since the early decades of the last century. Early theoretical work was motivated principally by rock and mineral crushing technology along with mining and quarry blasting applications. This historical work is not summarized here. However, a recent review addressing this history is scheduled for publication in the near future and is recommended [Grady, 2006]. Much of the effort of earlier workers [*e.g.*, Gaudin, 1926; Bennett, 1936; Lienau, 1936; Gilvarry, 1961; Gaudin and Meloy, 1962] focus on the characterization of brittle fracture through a Poisson statistical process. This approach to the statistics of brittle fragmentation now appears to be in error.

Some understanding of the statistics of brittle fragmentation is achieved through intriguing parallels of the dynamic fragmentation of brittle solids with hydrodynamic turbulence in fluids. Since the latter is still regarded as one of the remaining unsolved problems of classical physics, it is perhaps not surprising that a satisfactory statistical theory of brittle fracture and fragmentation continues to elude a sound theoretical basis

### *Hydrodynamic Turbulence*

Turbulence can occur in fluids described by the Navier-Stokes equations where governing material properties are relatively few in number. A macroscopic length scale  $L$ , a characteristic velocity  $V$ , and a viscosity  $\eta$  are adequate to reveal the essential features. The length  $L$  is, for example, the size of the structure imparting motion to the fluid while  $V$  is the nominal velocity impressed on the fluid. When the dimensionless Reynolds number  $R_e = LV / \eta$  is sufficiently large turbulence arises in the fluid motion.

Turbulence in the flow emerges because large scale laminar flow is not sufficient to dissipate the energy through viscous friction. Turbulence is then the activation, the growth, and the motion, of irregular fluid disturbances on successively smaller length scales necessitated by dissipation requirements of the fluid. The essence of turbulence is the transient and steady state motion of a hierarchy of submotions over a wide range of length scales. This cascade to successively smaller length scales in the turbulence process proceeds until velocity gradients of order  $V / \lambda$  are achieved that are adequate to support the necessary viscous dissipation. The range of length scales between  $L$  and  $\lambda$  is determined by the Reynolds number and increases with increasing Reynolds number.



The range of submotions of length scales bounded by  $L$  and  $\lambda$ , and reasonably removed from either is commonly called the inertial range [e.g., Falkovich and Sreenivasan, 2006]. Invariance to scale and self-similar physics is expected within the inertial range. Kolmogorov (1941) argued for such scale invariance on dimensional grounds, and arrived at a power law dependence of features of the turbulent motions on length scale over the inertial range. Recent theoretical work on turbulence suggests that the scale invariance of Kolmogorov is not fully realized [Chen *et al.*, 2005]. For present purposes, however, such scale invariance, or near-scale invariance, is a crucial observation of hydrodynamic turbulence, and offers a perspective for understanding the nature of dynamic brittle fragmentation.

## Catastrophic Fracture

Striking parallels to hydrodynamic turbulence are seen in the catastrophic fracture and fragmentation of brittle solids. Consider a solid object of characteristic size  $L$  composed of brittle material such as glass or a high-strength ceramic that is subjected to a compressive load inducing a nominal elastic specific strain energy  $\mathcal{E}$ . Natural fracture of the object initiates when critical stress conditions are achieved at some site in the body. Once initiated fracture proceeds rapidly and explosively, converting the elastic strain energy into surface fracture energy  $\gamma$  and kinetic energy of the ejected fragments.

Fracture in brittle solids is weakly dissipative, however, and failure through one or several through-going cracks is far from adequate to absorb the initial stored elastic strain energy. Consequently, during failure, fracture on successively finer length scales progresses through a cascade of crack branching until a length scale adequate to the dissipation of the initial elastic strain energy is achieved. This length scale is expected to scale as  $\lambda \sim \gamma / \rho \mathcal{E}$ , with  $\rho$  the material density. This limiting length scale  $\lambda$  is a number of decades smaller than the characteristic size  $L$  of the body.

Within the inertial range  $\lambda < x < L$  there is no length scale governing the physics of the catastrophic fracture cascade. Consequently, the fragment count within this range is expected to exhibit a power-law dependence on fragment size. As fragment size approaches the limiting dissipation length scale  $\lambda$  the functional dependence will diverge from the power-law dependence exhibiting an *impending awareness* of the dissipation limit length scale  $\lambda$ .

Although the specific functional form for the fragment number distribution is not known, an appropriate relation for the number distribution is readily guessed. The functional form,

$$N(x) = \frac{N_o}{1 + (x/\lambda)^\delta}, \quad (53)$$

exhibits the necessary power-law dependence for  $x \gg \lambda$  and the appropriate impending awareness within the range  $x \sim \lambda$ .  $N(x)$  is the complementary cumulative number

distribution (number greater than) of fragments while  $N_o$  is the total number of fragments. The total fragment number will be replaced with  $N_o = a_o (\sigma / \lambda)^\delta$ . Equation (53) becomes,

$$N(x) = a_o \frac{(\sigma / \lambda)^\delta}{1 + (x / \lambda)^\delta}, \quad (54)$$

and in the inertial range  $x \gg \lambda$ ,

$$N(x) = a_o (\sigma / x)^\delta. \quad (55)$$

The exponent  $\delta$  is the fractal dimension for the power-law representation of the cumulative fragment relation in Equation (55). The coefficient  $a_o$  is a number of order unity and is determined by normalization to the total mass of the body.

The quotient  $\sigma / \lambda$  in Equation (54) is the dimensionless ratio of the two limiting length scales of the distribution. This number is thought to be an important feature of the theory. The number is the ratio of a largest statistical fragment size  $\sigma$ , which is dependent on the system size  $L$ , and the limiting dissipation length scale  $\lambda$ . This number determines the magnitude of the inertial range. It will be large; say  $\sigma / \lambda \approx 10^n$  where  $n$  may range from several to perhaps 10 or more. The extent of the inertial range will be identified by its magnitude in powers of ten as “ $n$ -log size reductions”.

A cumulative probability distribution for the statistical relation follows from Equation (53),

$$P(x) = 1 - N(x) / N_o = \frac{(x / \lambda)^\delta}{1 + (x / \lambda)^\delta}, \quad (56)$$

and with probability density,

$$p(x) = \frac{\delta}{\lambda} \frac{(x / \lambda)^{\delta-1}}{(1 + (x / \lambda)^\delta)^2}. \quad (57)$$

From Equation (53) or (56) the fragment number increment in the range  $x \gg \lambda$  is,

$$dN = N_o \frac{\delta}{\lambda} \left( \frac{\lambda}{x} \right)^{\delta+1} dx. \quad (58)$$

Introducing a fragment mass  $\rho x^3$  the mass of fragments of size  $x$  within increment  $dx$  is,

$$dM = \rho x^3 dx = \frac{\delta}{\lambda} N_o \rho x^3 \left( \frac{\lambda}{x} \right)^{\delta+1} dx, \quad (59)$$

and cumulative mass to size  $x$ ,

$$M(x) = \delta N_o \rho \lambda^3 \int_0^x \frac{1}{\lambda} \left( \frac{\lambda}{x} \right)^{\delta-2} dx, \quad (60)$$

or,

$$M(x) = \frac{\delta}{3-\delta} N_o \rho \lambda^3 \left( \frac{x}{\lambda} \right)^{3-\delta}. \quad (61)$$

The integral in Equation (60) incurs a negligible mass error in ignoring the form of the function near  $x \approx \lambda$ . A requirement of  $M(\sigma) = M_o = \rho L^3$ , the total mass of the body at  $x = \sigma$  constrains the expression for  $N_o$  introduced above. Equation (61) at  $x = \sigma$  yields,

$$M_o = \rho L^3 = \frac{\delta}{3-\delta} N_o \rho \lambda^3 \left( \frac{\sigma}{\lambda} \right)^{3-\delta}. \quad (62)$$

Solving for  $N_o$ ,

$$N_o = \frac{3-\delta}{\delta} \frac{L^3}{\sigma^3} \left( \frac{\sigma}{\lambda} \right)^{\delta} = a_o \left( \frac{\sigma}{\lambda} \right)^{\delta}, \quad (63)$$

provides the coefficient  $a_o$ . Equation (61) is then,

$$M(x) = M_o \left( \frac{x}{\sigma} \right)^n, \quad (64)$$

in the form of the classic Schuhmann equation [Schuhmann, 1940] where  $n = 3 - \delta$ .

Identifying the surface area of a fragment of size  $x$  as  $6x^2$  the incremental distribution surface area is,

$$dA = 6x^2 dN = 6\delta \lambda N_o \left( \frac{\lambda}{x} \right)^{\delta-1} dx. \quad (65)$$

The cumulative fragment surface energy less than size  $x$  is provided by the integral,

$$A(x) = 6\delta \lambda^2 N_o \int_{\lambda}^x \frac{1}{\lambda} \left( \frac{\lambda}{x} \right)^{\delta-1} dx. \quad (66)$$

## **Turbulence at the Tip of a Fast-Running Crack**

Similarities between hydrodynamic turbulence and catastrophic brittle fracture also are evident in the propagation of a single crack. The laminar flow of a rapidly shearing fluid soon becomes unsettled by the emergence of insipient eddies and vortices as the intensity of shearing is increased. Again, dissipation through laminar viscosity is increasingly inadequate to balance the power input. Energy dissipated at the tip of a fast running crack in a brittle solid is known to be a strong function of the velocity of the crack. Increased dissipation is a consequence of the onset microcrack branching instability at sufficiently high velocity [Sharon *et al.*, 1991]. Again, microcrack instability is the physical equivalent of hydrodynamic turbulence exhibited by the crack in exploring crack-tip deformations capable of the needed dissipation.

## VI Closure

Application of the ideas put forth in the last section on the catastrophic failure and fragmentation of brittle solids to the ballistic performance of ceramics is far from clear. In the several pages presented, we have just scratched the surface of some of the issues on the failure and the nature of the failed material as it may relate to armor performance. It is generally recognized that in the terminal ballistic event material in intimate contact with the penetrating body, and providing the resistance to penetration, is probably failed and highly fractured ceramic. The specific makeup of the failed ceramic is not known, however, and this characterization of the ceramic may be important to the resisting strength of the material.

Catastrophic failure, leading to the very fine comminution of the ceramic, is directly linked to the magnitude of elastic strain energy achieved before failure of the ceramic ensues. An abstraction of the sequence of events occurring as a high velocity kinetic energy penetration proceeds in ceramic is illustrated in Figure 19. An element of the ceramic impeding the progress of penetration is identified in the figure. Key states of this ceramic element, as penetration resistance and failure proceeds, are shown. The element is first illustrated at rest and unstrained ahead of the approaching pressure wave accompanying the steady penetration. As the pressure wave subsumes the element, elastic strain energy builds until brittle failure of the element occurs. Strain energy will fuel explosive fracture of the element. Intensity of catastrophic fracture is determined by the magnitude of strain energy achieved in the element preceding failure.

Failure of the element will occur when the propagating fracture front reaches the ceramic element. Thus, delaying kinetics of the fracture activation and growth is explored in some detail in the first technical section of the present report and will play a crucial role in determine the level of strain energy achieved before failure. Time-dependent fracture is modeled in this section with a physically sensible statistical meso-kinetic representation of the material response under the intense pressure wave loading. Failure at sites of weakness in the heterogeneous ceramic requires the time-dependent development of stress concentration as elastic strain equilibrates following the rapid pressure loading.

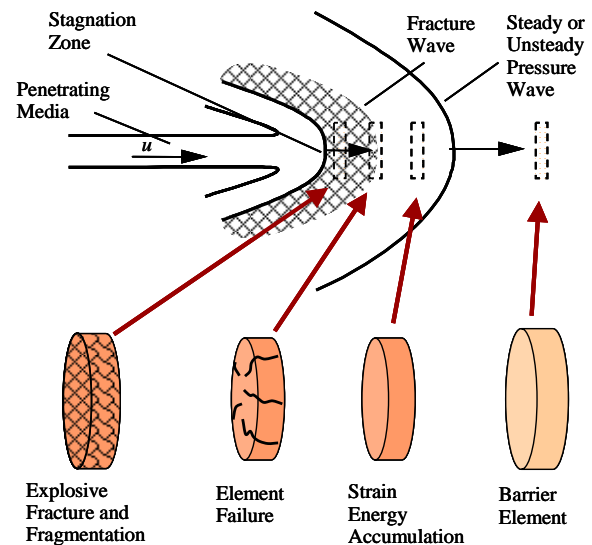


Figure 19: The sequence of stress-wave loading, ballistic resistance, failure, and catastrophic fragmentation of an element of armor ceramic.

There are reasons to believe that a time-dependent Tuler-Butcher failure criterion would adequately model the phenomenological aspects of the ceramic resistance and failure in the ballistic event. The development of a physical model for the impact failure of ceramic plate

using the Tuler-Butcher criterion in the second technical section, and the comparison with available data on the impact breach of glass plate, suggests such a modeling approach is appropriate. Application to a wider range of terminal ballistic resistance and failure phenomena seems reasonable.

The dependence of the post-failure strength of the ceramic on fragment size and distribution of the failure-generated debris is not known. The fracture strength of a single brittle particle, however, is known to depend on the size of the particle – increasing as the particle size decreases. Thus, it is sensible to expect the shear resistance of comminuted ceramic to depend on the distribution of particle size. Further, shear resistance should probably increase with deformation as the distribution particle size of the comminuted material is further reduced.

A dependence on the shape of the distribution, say the power exponent if a power-law description of the distribution, however, is not intuitive. The importance of such details will only be uncovered through a deeper investigation of the underlying physics.

## VII References

1. Bennett, J. G., (1936) *Broken Coal*, J. Inst. Fuel, 10, 22-39.
2. Bourne, N. K., Z. Rosenberg, Y. Mebar, T. Obara, and J. E. Field, (1994) *A High Speed Photographic Study of Fracture Wave Propagation in Glass*, DYMAT 94 International Conference on Mechanical and Physical Behaviour of Materials under Dynamic Loading, les Editions de Physique, pp. 635-640.
3. Brannon, O. J., C. Conrad, R. W. Morris, E. D. Jones, J. R. Asay, (1983) *Studies of the Spectral and Spatial Characteristics of Shock Induced Luminescence from X-Cut Quartz*, J. Appl. Phys., 54, 6374-6381.
4. Chen, S. (2005) J. Fluid Mech., 533, 183.
5. Falkovich, G. and K. R. Sreenivasan, (2006) *Lessons from Hydrodynamic Turbulence*, Physics Today, April, 43-49.
6. Freund L. B., (1990) *Dynamic Fracture Mechanics*, Cambridge University Press, New York.
7. Galanov, B. A., O. N. Grigor'yev, V. V. Kartuzov, V. N. Ostapenko, V. I. Trefilov, (1989) *Impact Failure of Ceramic Plates*, Sov. Powder Metall. Ceram., 4, 299.
8. Gaudin, A. M., (1926) *An Investigation of Crushing Phenomena*, AIME Trans., 73, 253-316.
9. Gaudin, A. M., and T. P. Meloy, (1962) *Model and a Comminution Distribution Equation for Single Fracture*, AIME Trans., 223, 40-43.
10. Gilvarry, J. J., (1961) *Fracture of Brittle Solids. I. Distribution Function for Fragment Size in Single Fracture (Theoretical)*, J. Appl. Phys., 32, 391-399.
11. Grady, D. E., (1981) *Fragmentation of Solids Under Impulsive Stress Loading*, J. Geophys. Res., 86, 1047-1054.
12. Grady, D. E., (1988) *The Spall Strength of Condensed Matter*, J. Mech. Phys. Solids, 36, 3, 353-384
13. Grady, D. E., (1995) *Shock Properties of High-Strength Ceramics*, in Constitutive Laws: Theory, Experiment and Numerical Implementation, A. M. Rajendran and R. C. Batra, eds., CIMNE, Barcelona, pp. 35-45.
14. Grady, D. E., (1998) *Shock Wave Compression of Brittle Solids*, Mech. Materials, 46, 181-203.
15. Grady, D. E., (2005) *Analysis of Shock and High-Rate Data for Ceramics: Physics Based Models for Armor Ceramics*, Prepared for, U.S. Army TARDEC, Applied Research Associates Tech. Rept., March.
16. Grady, D. E., (2006a) *Fragmentation of Rings and Shells: The Legacy of N. F Mott*, Springer-Verlag, New York.

17. Grady, D. E., (2006b) *Dynamic Fragmentation of Solids*, in Shock Wave Handbook: Shock Waves in Solids, Y. Horie, editor, to be published.
18. Grady, D. E., and L. C. Chhabildas, (1997) *Shock-Wave Properties of Soda-Lime Glass*, Proceedings, 4<sup>th</sup> U. S. Symposium on Solid Mechanics, Myrtle Beach, SC, October 16-18, 1996, Batelle Press, 29-38.
19. Grady, D. E., R. E. Hollenbach, K. W. Schuler, and J. F. Callender, (1977) *Strain Rate Dependence of Dolomite Inferred from Impact and Static Compression Studies*, J. Geophys. Res. 82, 8, 1325-1330.
20. Holmquist, T. J. and G. R. Johnson, (2002) *Response of Silicon Carbide to High Velocity Impact*, J. Appl. Phys., 91, 5858-5866.
21. Holmquist, T. J. and G. R. Johnson, (2006) *Characterization and Evaluation of Boron Carbide from One-Dimension Plate Impact*, to be published.
22. Kanel, G. I., Rasorenov, S. V., Fortov, V. E., (1992) *The Failure Waves and Spallation in Homogeneous Brittle Materials*, Shock Waves in Condensed Matter - 1991, Elsevier Science Publ., pp. 451-454.
23. Kolmogorov, A. N., (1941) Dokl. Akad. Nauk. SSSR 30, 9 & 32, 16; reproduced in Proc. R. Soc. London, Ser. A 434, 9 (1991).
24. Lawn, B., (1993) *Fracture of Brittle Solids – Second Edition*, Cambridge University Press.
25. Lienau, C. C., (1936) *Random Fracture of a Brittle Solid*, J. Franklin Inst., 221, 485-494, 674-686, 769-787.
26. Mott, N. F. (1947), *Fragmentation of Shell Cases*, Proc. Royal Soc., A189, 300-308, January.
27. Niesz, D. E., (2005) *High Fidelity Design and Processing of Advanced Armor Ceramics*, Eight Semi-Annual Progress Report, Rutgers State University, New Jersey.
28. Schuhmann, R., (1940) *Principles of Comminution, I., Size Distribution and Surface Calculations*, AIME Tech. Publ. 1189, Mining Technology, 1-11.
29. Sharon, E., S. P. Gross, J. Fineberg, (1996) *Energy Dissipation in Dynamic Fracture*, Phys. Rev. Letters, 76, 2117-2120.
30. Sun, X., M. A. Khaleel, R. W. Davies, (2006) *Modeling of Stone-impact Resistance of Monolithic Glass Ply Using Continuum Damage Mechanics*, Int. J. Damage Mech.
31. Tuler, F.R., and B.M. Butcher, (1968) *A Criterion for the Time Dependence of Fracture*, Int. J. Fracture Mech., 4, 431-437.
32. Vogler, T. J., W. D. Reinhart, L. C. Chhabildas, (2006) *Dynamic Behavior of Boron Carbide*, J. Applied Phys., 95, 4173-4183.
33. Weibull, W., (1951) *A Statistical Distribution Function of Wide Applicability*, J. Appl. Mech., 18, 293.